

## Experimental investigation of flow around a 45° oriented cube for Reynolds numbers between 500 and 50 000

Majid Hassan Khan , P. Sooraj , Atul Sharma , and Amit Agrawal <sup>\*</sup>  
*Department of Mechanical Engineering, Indian Institute of Technology Bombay,  
Mumbai, Maharashtra 400076, India*



(Received 19 June 2020; accepted 22 June 2021; published 15 July 2021)

Flow around an oriented cube is experimentally studied using particle image velocimetry measurements. The cube is rigidly suspended and oriented at an angle of 45° with respect to the freestream flow. Instantaneous and mean flow fields in the wake have been examined at 16 different values of Reynolds numbers between 500 and 50 000. Vorticity identified using swirling strength shows a chaotic wake at higher Re. A wider wake and a longer wake length are noted as compared to flow around a normal cube. The wake width collapses to nearly the same value for all Re beyond the wake length. Unlike a cube, an oriented cube has a recirculation region with multiple peaks for velocity deficit, which is a signature of many smaller eddies present in the wake. The range of investigated Reynolds numbers shows behavioral changes in the wake, hinting at the possibility of critical Reynolds numbers (or different regimes) based on a maximum velocity deficit, maximum vorticity magnitude, and energy content of the first mode extracted using proper orthogonal decomposition. Proper orthogonal decomposition has been used to understand the contribution of different modes in the formation of coherent structures in the wake. An oriented cube is an extreme case for nonspherical objects and has marked differences from the wake of a cube and other regular-shaped objects. The present work is an attempt to provide an understanding of and improve upon the scarce investigation performed for the wake of an oriented cube.

DOI: [10.1103/PhysRevFluids.6.074606](https://doi.org/10.1103/PhysRevFluids.6.074606)

### I. INTRODUCTION

Flow around obstacles, whether mounted or freely suspended, are not always simplistically oriented normal to the body. The orientation of the body varies with respect to the flow direction. Orientation plays a significant role in the fluid dynamics of the wake. Wakes of two-dimensional bluff bodies are affected by the orientation or inclination in the plane of the flow, but finite-size three-dimensional bluff bodies have a volumetric effect on the flow. Square cylinders and cubes are the simplest model examples of bluff bodies with noncircular cross-sectional geometry whose orientation affects the flow. Orientation of a cube with respect to the flow is the bluff body considered for the present work. This work is an extension of our earlier work [1], which investigated flow around a cube.

Flow around a cube has a square cylinder as the nearest counterpart in two-dimensional flows. References [2–4] are a few of the representative works done for flow around square cylinders. Vortex shedding for a square cylinder starts around Reynolds number  $Re = 50$  [4] and the flow becomes three dimensional between  $Re = 150$  and  $Re = 175$  [5]. The inclination of a square cylinder affects the wake dynamics. Sohankar *et al.* [6] reported unsteady flow for an oriented square cylinder for Re

---

<sup>\*</sup>amit.agrawal@iitb.ac.in

between 45 and 200. They reported a smooth increase in Strouhal numbers for angles of incidence from  $0^\circ$  to  $45^\circ$ . The drag coefficient for an angle of  $45^\circ$  is more than a normally placed square cylinder. Ozgoren [7] compared the flow physics of a circular cylinder, a square cylinder, and a  $45^\circ$  oriented square cylinder for  $550 \leq Re \leq 3400$  and reported larger wakes with more rotational fluid motion in the wake of the oriented square cylinder. Ozgoren [7] reported that the wake of an oriented cylinder has a higher number of small-scale vortices. Dutta *et al.* [8] also showed an increase in wake size for inclinations greater than zero and reported that the separation points moved downstream for  $Re = 1340, 4990, \text{ and } 9980$ . Dutta *et al.* [9] showed the dependence of wake size on orientation, proposing  $22.5^\circ$  as the critical orientation for lower drag coefficient  $C_d$  and higher Strouhal number. They reported a decrease in drag coefficient with an increase in aspect ratio and showed that  $C_d$  for aspect ratio 16 is greater for an orientation of  $45^\circ$  as compared to the normal arrangement of a square cylinder. van Oudheusden *et al.* [10] used proper orthogonal decomposition for particle image velocimetry (PIV) measurement of flow around a square cylinder at  $Re = 4000, 10\,000, \text{ and } 20\,000$  to report the dependence of vortex shedding on different angles of incidence. van Oudheusden *et al.* [11] reported the flow topology and wake behavior for angles of orientation  $0^\circ, 5^\circ, 10^\circ, \text{ and } 15^\circ$ . Tong *et al.* [12] used PIV measurements at different orientation in the unsteady regime for  $Re$  between 60 and 350 to identify two modes of instabilities in the wake of an inclined square cylinder. Huang *et al.* [13] proposed three critical regimes for different angles of orientation ( $\alpha$ ) for a square cylinder: (i) subcritical ( $0 \leq \alpha < 15^\circ$ ), (ii) supercritical ( $15^\circ \leq \alpha < 45^\circ$ ) and (iii) wedge ( $\alpha = 45^\circ$ ). Yoon *et al.* [14] showed an enhanced heat transfer in a channel flow by using a square cylinder oriented at  $45^\circ$ . Similar heat transfer enhancement was also shown by Moussaoui *et al.* [15] using a multiple-relaxation-time lattice Boltzmann equation for a  $45^\circ$  oriented square cylinder in a horizontal channel. A finite-size square cylinder has a three-dimensional wake and cube is a special case of square cylinder with aspect ratio 1.

Flow around surface mounted cubes and cuboids, which served the purpose of understanding flow around finite-size three-dimensional obstacles near a surface, were presented by, e.g., Castro and Robins [16], Hunt *et al.* [17], and Hosker [18]. Surface mounted obstacles have horseshoe vortices due to a shear layer interacting with the boundary layer. The present work provides an understanding of the flow around an oriented cube suspended with all sides free to the flow except for a mount on one side. Earlier works for flow around a normal cube include a cube drop experiment [19], numerical simulations [20–22], and PIV measurements [1,23]. Saha [21] identified three flow regimes at moderate Reynolds numbers: (i) steady symmetric ( $Re < 215$ ), (ii) steady asymmetric ( $218 \leq Re \leq 265$ ), and (iii) unsteady flow ( $Re > 270$ ). Khan *et al.* [24] used three-dimensional lattice-Boltzmann-method-based numerical simulation to categorize the flow in four regimes based on flow structures for  $Re$  between 84 and 770. Khan *et al.* [25] explained the hairpin vortex shedding for a cube and elucidated the flow structures for  $Re$  in different regimes identified by Khan *et al.* [24]. A PIV measurement was done by Klotz *et al.* [23] for flow around a cube at moderate Reynolds number between 100 and 400 confirming two flow bifurcations. All the previous work for flow around a suspended cube was limited to moderate Reynolds numbers. Khan *et al.* [1] presented the flow behavior for the cube at higher  $Re$  between 500 and 55 000. Unlike flow around an oriented square cylinder, there is a dearth of work on flow around a cube oriented with respect to the freestream.

The non-normal fluid-cube interaction becomes an important domain of investigation with the cube oriented at  $45^\circ$  as a special case. Richter and Nikrityuk [26] investigated the effects of the orientation of a cube on the force coefficients for  $Re$  between 10 and 200. Klotz *et al.* [23] briefly mentioned their preliminary study on the effect of cube rotation with respect to the freestream at  $Re = 250$  and 330. Hölzer and Sommerfeld [27] explained that the nonspherical particles have higher drag for an arrangement with a maximum projected area normal to the flow, which for the cube is an orientation of  $45^\circ$  with respect to the freestream flow. This creates a need to investigate the physics in detail for a cube oriented at  $45^\circ$  with respect to the freestream.

The present work explains the object-flow configuration where the cube is oriented at  $45^\circ$  at various higher Reynolds numbers and gives a comparison with flow around a cube [1]. Nonspherical

TABLE I. Tunnel specifications.

Tunnel component	Value
Induction (main) motor	5.5 kW, 722 rpm
Geared motor	0.37 kW, 29 rpm
Contraction ratio	9:1
Test section (glass)	1500 × 400 × 400 mm <sup>3</sup>
Flow parameter	Value
Velocity range	0.011–2 m/s
Turbulent intensity	<2%

objects are predominant for applications based on immersed obstacles in a flow and their orientation defines the wake behavior. A 45° oriented cube is the extreme case of cube orientation with respect to the freestream. A larger-size wake with better mixing ability, higher drag coefficient, and different turbulent statistics, which can be of immense technological use, provide reasons for a detailed investigation. The present work has been done with the specific objectives to (i) examine the wake of an oriented cube, (ii) examine the mean and turbulent flow behavior at different axial locations, (iii) analyze the effect of various Reynolds numbers in the unsteady regime, (iv) compare the wake of an oriented cube with the wake of a normal cube, and (v) analyze the energy content of various modes along with their role in coherent structure reconstruction using proper orthogonal decomposition. Particle image velocimetry measurements were conducted in a water tunnel for  $Re \in (500, 50\,000)$  for a cube oriented at 45° to the streamwise flow.

## II. EXPERIMENTAL SETUP AND DATA ANALYSIS

Particle image velocimetry measurements were performed for flow around an oriented cube mounted in a closed circuit water tunnel. A description of the water tunnel was presented earlier in Ref. [1] for measurements of flow around a rigidly suspended normal cube. The specifications are listed in Table I.

The present work focuses on flow around an oriented cube and draws a comparison with the earlier work on flow around a normal cube [1]. Experiments were conducted for 16 different Reynolds numbers using a cube oriented at 45° with respect to the flow. The cube has side length of 40 mm and is made of transparent acrylic. When seen from the top, the oriented cube appears as a rhombus aligned with the axis along the flow direction and mounted at the center of the top face. This arrangement kept the separating edge free from any obstruction due to the holder used as a mount. The wedge-shaped separation edge and the sides were of interest for the flow investigation, so the cube was mounted with a thin straight rod from the top. Images obtained from PIV measurements were analyzed using cross correlation and the obtained result was calibrated to get the flow field in physical dimensions. The extracted flow field was analyzed to explain the physics in the wake of an oriented cube. The swirling strength was calculated from velocity data to study the vortical structures quantitatively [defined later through Eq. (7)]. Proper orthogonal decomposition was used to extract various modes and get insight into the coherent structures corresponding to the extracted modes. The following sections explain the PIV measurement system employed, PIV image analysis, and proper orthogonal decomposition used to analyze the flow field.

### A. The PIV measurement system

Particle image velocimetry (specifications in Table II) employed for the present case was similar to that used in Refs. [1,28–30]. Figure 1(a) shows schematically an arrangement of the oriented cube in the test section of the water tunnel along with the laser sheet, camera, and flow direction.

TABLE II. Particle image velocimetry specifications.

PIV hardware and accessories	
Laser	Nd:YAG 532-nm wavelength Pulse widths of 7.7 and 6.8 ns Beamtech Vlite-200
Synchronizer	Beamtech
Camera	CCD, PCO, Germany 1024 × 1392 pixels Frame rate of 10 Hz
Particle	Fused borosilicate glass Size of 8–9 μm Specific gravity 1.1
PIV evaluation	
PIVLAB [31,32]	MATLAB-based open-source package

The laser sheet passes through the midplane of the cube [Figs. 1(b) and 1(c)]. A CCD camera is placed normal to the sheet. The laser and camera are controlled using transistor-transistor logic signals from a synchronizer connected to a personal computer. A total of 907 pairs of images were recorded at 1 Hz, which is a data set of more than 15 min. The flow was checked for statistical convergence using a cumulative mean field and it was found to converge for an ensemble data

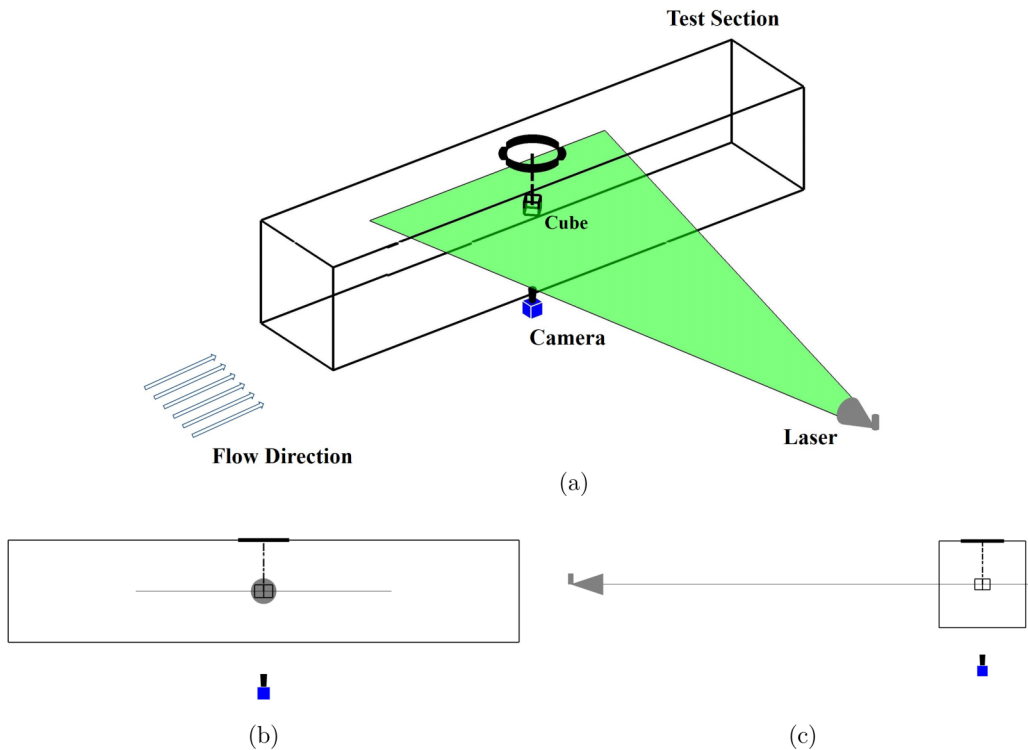


FIG. 1. (a) Schematic of the test section and PIV setup with the mounted cube arrangement. Also shown are (b) the alignment of the camera and (c) the alignment of the laser and camera.

of 250 images recorded at 1 Hz. In order to have lower sampling error, the present work uses an amount of ensemble data more than three times that required for statistical convergence. Since the data acquisition was done at 1 Hz, we have not been able to estimate the Strouhal number using the present set of measurements.

### B. The PIV image analysis

PIVLAB, a MATLAB-based open-source package [31,32], was used to analyze the images. In-house-developed MATLAB scripts were used for postprocessing the data and for estimating various parameters reported in this article. Cross correlation was done using an interrogation window of  $32 \times 32$  pixels and an overlap of 50%. Around 5400 velocity vectors were identified with a vector separation of 2 mm in the measured field of view of  $13 \times 18 \text{ cm}^2$ . The Stokes number is of the order of  $10^{-3}$  (i.e., much less than unity), showing that the tracer particles faithfully follow the streamlines.

The uncertainty in measurement of the velocity was estimated for image processing, particle lag, sampling, and the equipment [33]. The algorithm processing uncertainty is 0.5%. The particle lag is negligibly small given that the Stokes number is approximately  $10^{-3}$ . Sampling uncertainty is estimated to be 0.9% for lower Reynolds number and 0.6% for higher Re. Since sampling uncertainty is dependent on the standard deviation and average velocity, differences in the estimated uncertainties are noted with Re. Equipment uncertainty in the scaling factor is 0.6%, whereas uncertainty in the separation of time is negligibly small (of order  $10^{-6}$ – $10^{-8}$  %). The total uncertainty in the velocity measurement is 1.7–2 %.

### C. Proper orthogonal decomposition of flow fields

Since particle image velocimetry measurements give data which are whole field and are recorded for a finite time, deconstructing the complexity of the flow in individual units becomes important to understand the flow better. Proper orthogonal decomposition (POD) provides the basis to decompose the flow field in different modes with a certain portion of the total energy in each mode. The basic idea is to take a field  $\mathbf{U}$  and extract the fluctuating component as

$$\mathbf{U}(x, t) = u_{\text{mean}}(x) + u'(x, t). \quad (1)$$

Proper orthogonal decomposition creates a set of projections for an uncorrelated data set  $u'(x, t)$  onto an orthogonal set  $\{\phi_1, \phi_2, \dots, \phi_N\}$  such that the difference between the fluctuating component and the summation of  $N$  orthonormal basis projections calculated as

$$\epsilon = \sqrt{\|u'(x, t)\|^2 - \sum_{m=1}^N c_m^2 \|\phi_m\|^2} \quad (2)$$

is a minimum. The orthogonal basis should satisfy the criterion that  $\langle \phi_i, \phi_j \rangle = 0$  for all  $i \neq j$ . For  $\epsilon \rightarrow 0$ , i.e., when the projection converges to the given functions (Parseval's equality), Eq. (2) gives

$$u'(x, t) = \sum_{m=1}^N c_m \phi_m. \quad (3)$$

Using the variational approach, Holmes *et al.* [34] showed that when  $\epsilon \rightarrow 0$ , Eqs. (2) and (3) are an eigenvalue problem where

$$\mathcal{R}\phi = \lambda\phi, \quad (4)$$

where  $\mathcal{R}_{i,j} = \langle u'_i u'_j \rangle$ , whereas for a degenerate case  $\mathcal{R}_{i,j} = \frac{1}{N} \sum u'_i u'_j$ .

Since the data in particle image velocimetry have more spatial values (grid data) than the number of temporal images, the method of snapshots [35] becomes an optimum choice, as suggested by Chen *et al.* [36]. In the method of snapshots, a discrete PIV data set taken at different time

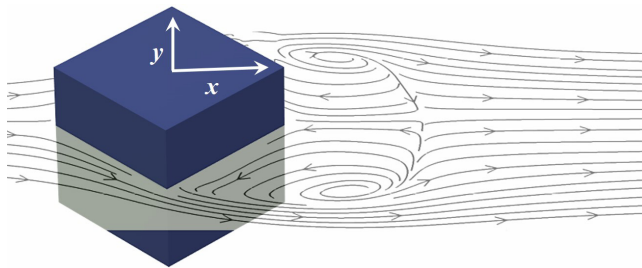


FIG. 2. Schematic showing the flow direction, the origin for all results for an oriented cube.

steps is used as snapshots. This process is quicker than the direct method. The snapshot method uses an approximation of the eigenfunction as a linear combination of the observable velocity field [35]. As each observation can be expressed as a linear combination of eigenfunctions with positive eigenvalues, similarly each eigenfunction can be represented by a linear combination of observations [34,37]:

$$\phi = \sum_{i=1}^N A_i u^{(i)}. \quad (5)$$

Using this value of  $\phi$  in Eq. (4), one gets an eigenvalue equation for the coefficients  $A_i$ ,

$$\sum_{i=1}^N \frac{1}{N} (u'_i u'_j) A_i = \lambda a_j, \quad j = 1, 2, \dots, N. \quad (6)$$

Single-value decomposition is performed over the spatial correlation matrix generated using fluctuations in  $u$  and  $v$  velocities as mentioned in [36,37]. The eigenvalues obtained using the POD correspond to the kinetic energy of each mode. Proper orthogonal decomposition decomposes the flow in modes where the eigenvalues give the fraction of kinetic energy content in each mode (optimality). The eigenfunctions associated with a particular eigenvalue give an idea about the flow structure associated with that mode.

### III. RESULTS AND DISCUSSION

The cube side length  $D$  is taken as a characteristic length for calculating the Reynolds number and for normalizing the axial and transverse distances. Figure 2 shows the axes for an oriented cube oriented at an angle of  $45^\circ$  to the flow;  $x$  and  $y$  are streamwise and transverse directions. Notice from the figure that the center of the cube has been chosen as the origin  $(0, 0)$  for ease of comparison between a normal and an oriented cube.

The following section discusses the instantaneous velocity for a flow around an oriented cube. The flow physics for an oriented cube is explained using time-averaged vector plots, isoregions of swirling strength, and streamlines. The physics in the wake is further studied by observing the flow behavior in the transverse direction at various axial locations. Time-averaged mean velocity profiles and normalized root mean square velocity profiles are presented to understand the mean flow and the effect of fluctuations in the flow. The centerline velocity plot in the wake gives an idea about the recirculation length. Turbulent statistics are discussed using normalized root mean square velocities ( $U_{\text{rms}}$  and  $V_{\text{rms}}$ ) and Reynolds shear stress (RSS).

Additional PIV measurements were performed to ascertain the flow condition in the water tunnel before the start of the measurements. The velocity profiles (not presented) for the water tunnel without any obstacle showed uniform flow at all Reynolds numbers. Flow for the tunnel without

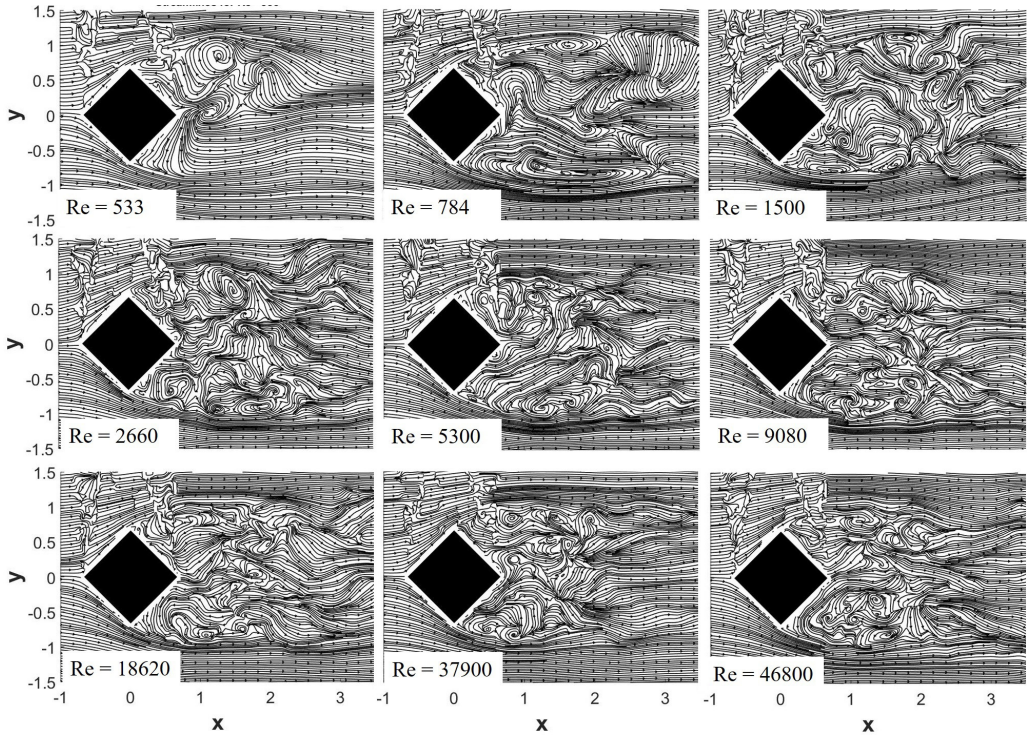


FIG. 3. Comparison of instantaneous streamlines for flow around an oriented cube at various Reynolds numbers.

any mounted object had near-zero values for RSS at all Re. This established that the background flow is uniform in the streamwise direction.

#### A. Instantaneous velocity

The nature of the wake is dependent on the obstacle geometry and the Reynolds number, which accounts for both the inertia of the flow and the viscosity of the fluid. Generally wakes are noted to have fully formed recirculating zones at lower Reynolds numbers for any bluff body in the steady regime and are mostly dominated by the viscous effects. At higher Reynolds numbers the inertial component dominates. The inertial component advects and stretches the recirculating zones. Figure 3 shows how the instantaneous wake behavior changes as the Reynolds number increases. We note larger eddies at  $Re = 533$  (Fig. 4). The wake has longitudinally stretched structures at  $Re = 784$  (Fig. 3). The wake region is larger at this Re as compared to  $Re = 533$  (Fig. 4). Beyond  $Re = 784$ , the structures in the wake are smaller since at higher Re the stretching leads to disintegration of the eddies into smaller ones. The wake for flow around an oriented cube blooms with many smaller structures for  $Re \geq 2660$ , the wake has many smaller structures, and the wake region is smaller than those at  $Re = 784$  and 1500. The wake region for higher Reynolds numbers of 18 620, 37 900, and 46 800 are chaotic and have many small recirculating zones. Figure 3 presents  $Re = 784$  as a critical Reynolds number after which the wake is filled with relatively smaller eddies and the axial distance with many smaller vortices is shorter compared to  $Re = 784$ . This inference is further supported by the identified vortical structure in the wake (Fig. 7) and the trend in recirculation length (Fig. 8). (Figure 11 will further elucidate the varying trends in the wake at various Re.) The temporal flow behavior is further analyzed for the wake of an oriented cube at  $Re = 784$ . It should be noted that the flow analysis in Fig. 3 and the following sections focuses on

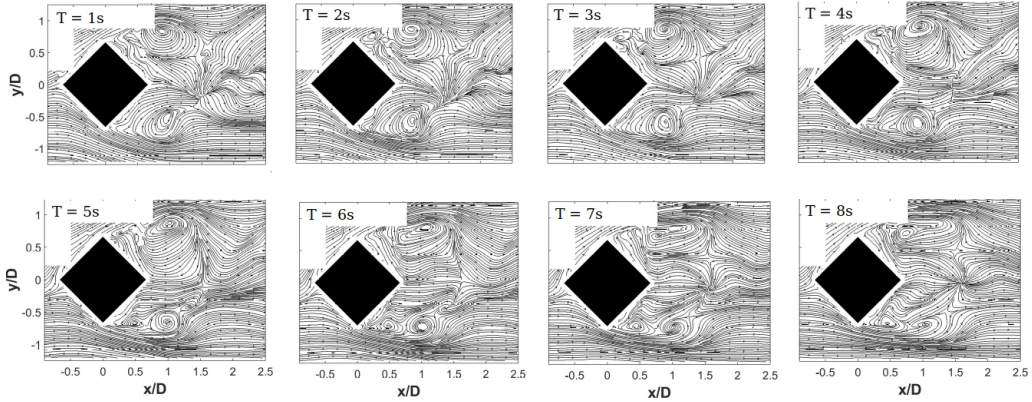


FIG. 4. Temporal variation of instantaneous streamlines for flow around an oriented cube at  $Re = 533$ .

the wake region only since the shadow region formed due to diffraction from the cube induces error in the velocity field in the region near the corners as shown in Fig. 5.

Streamlines for the instantaneous velocity field for  $Re = 784$  are shown in Fig. 6. Figures 6(a)–6(l) show the flow behavior for an arbitrarily chosen flow field of 12 s. For the presented instantaneous time frame we note that the maximum vortical action happens only in the upper half of the wake, i.e., towards one side of the centerline. The number of eddies found in the upper half of the frames is higher than that for the lower half. At later time instants (not presented here) the situation flips. This is due to the phased nature of the flow. Similar behavior was also observed for  $Re = 533$ .

The flow is tilted towards one direction and later it flips towards the other. Similar periodic nature has been reported for flow around a square cylinder placed normal to the flow direction at  $Re = 14\,000$  [38]. Although the present measurements have been done for the midslice of the three-dimensional flow around an oriented cube, the recirculating packets in the wake help explain the flow behavior. Perry and Chong [39] provided a framework and methodology of using critical points to explain the flow patterns in a three-dimensional flow. Almost all the frames have attracting

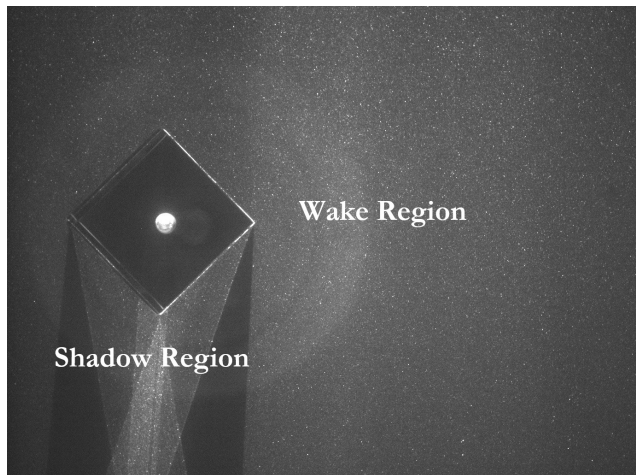


FIG. 5. Sample PIV image showing the wake region analyzed in this work and the shadow region on one side of the oriented cube due to diffraction at the corners.

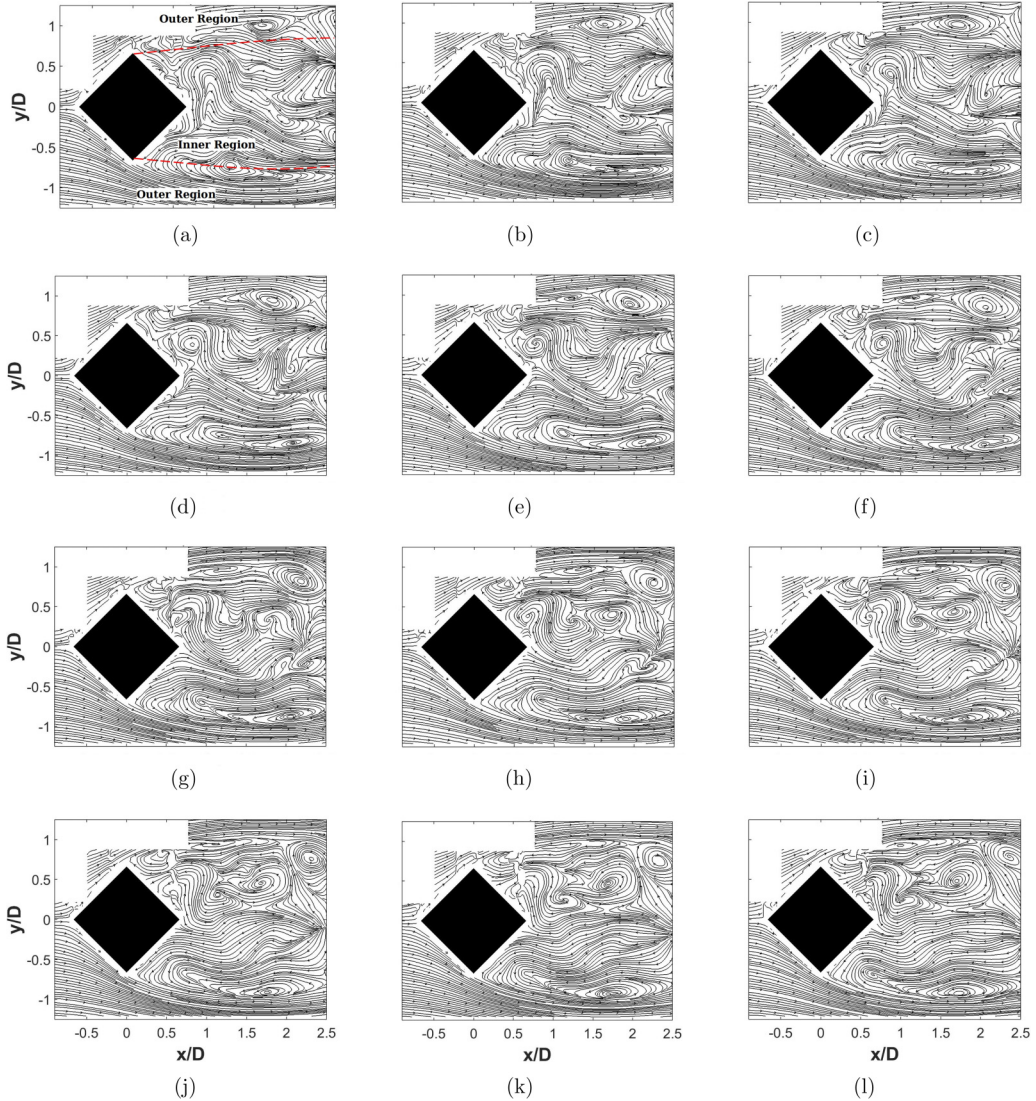


FIG. 6. Temporal variation of instantaneous streamlines for flow around an oriented cube at  $Re = 784$ : (a)  $t = 1$  s, (b)  $t = 2$  s, (c)  $t = 3$  s, (d)  $t = 4$  s, (e)  $t = 5$  s, (f)  $t = 6$  s, (g)  $t = 7$  s, (h)  $t = 8$  s, (i)  $t = 9$  s, (j)  $t = 10$  s, (k)  $t = 11$  s, and (l)  $t = 12$  s.

(streamlines moving inward toward a common region) and repelling (streamlines moving outward from a common region) nodes, along with focus (movement of streamlines is either inward or outward at a particular point) and saddle points (location with singularities where all streamlines are tangent). The rolling of the fluid in a three-dimensional space can be inferred from these repelling and attracting centers. The rolling of fluid shows how the streamlines move in and out of the plane. At the edge of the wake in the transverse direction the rolling of the shear layers into smaller recirculating regions is seen. Smaller recirculating regions are formed which slowly grow in size and are advected into the far wake region. The streamwise motion is added to the transverse diffusivity in the wake, which at later time instants is tilted in the opposite direction.

Notice that the region behind the cube experiences a reverse flow, while the flow is in the forward direction outside the wake. This shearing between the movement of oppositely flowing streams leads to the formation of vortices in the shear layer. The shear layer forms vortices at around  $1.5D$  from the center of the cube. Smaller vortices are formed for all the  $Re$  investigated in the present work. Since the flow is at higher  $Re = 784$ , many small vortical structures are formed, giving a sense of chaotic flow. The three dimensionality of the flow also leads to stretching and tilting of vortices. At  $Re = 533$  the vortical structures are bigger; they break down into smaller ones at  $Re \geq 784$ . The outer region of the wake (in the transverse direction as marked in Fig. 6 for  $t = 1$  s) has single vortices, whereas the inner region shows the presence of both paired and single vortices. The sizes of the vortices and recirculating region become smaller at higher Reynolds numbers. A broader wake is observed as compared to the wake of a normal cube [1].

The comparison of wake at different  $Re$  necessitates a discussion on how the mean velocity and vorticity fields behave. The following section presents the time-averaged velocity and vorticity fields to explain the behavior of the mean flow field in the wake of an oriented cube.

### B. Time-averaged velocity and vorticity

The deviation from the freestream flow marks the character of the wake. Understanding and analyzing the flow patterns of the streamwise velocity components aid in the kinematic understanding of the wake. Figure 7 shows the time-averaged velocity vectors for an oriented cube at various  $Re$  along with contours of swirling strength.

The region with velocity magnitude lower than the freestream velocity component gives an idea about the geometry of the wake. The streamwise velocity pattern of the wake explains the recirculation region and the region of velocity deficit. It helps us understand the rate of gain in the velocity deficit with respect to the axial location. The geometry of the wake is deciphered using the streamwise velocity vector plots.

Flow around an oriented cube has a blunter velocity deficit zone at  $Re = 533$ , as compared to the flow around a cube placed normal to the flow direction. At  $Re = 784$  the deficit zone increases in size and then decreases for higher  $Re$ . Similar behavior was noted for the instantaneous streamlines shown in Fig. 3. The geometry of the deficit zone differs from that of flow around a cube in terms of both shape and size. The zone around an oriented cube has multiple peaks of streamwise velocity and even the wake has more areal spread (Fig. 10). The wake for flow around a cube converges beyond the bluff body [1], whereas the wake for an oriented cube is initially bulged and then it closes to form a deficit zone with a flatter end or an end with multiple peaks. The shape of the lower velocity i.e., the negative zone for  $Re = 530$ , is flatter and has multiple peaks at  $Re = 18\,600$ . Such deficit zones of multiple peaks lose their symmetry at higher  $Re$ .

There is a change in velocity direction as one moves away from the cube in the axial direction. As explained in Ref. [1], the wake tapers to conserve momentum for flow around a cube. The change in sign of velocity at higher  $Re$  is at a lower  $x/D$  (closer axial distance) due to the higher inertia of the flow. The velocity vectors for flow around an oriented cube help us understand the flat profile and further elucidate profiles of multiple peaks of the velocity vector field of Fig. 7 and time-averaged streamwise velocity profiles of Fig. 10. The taper in the near wake region is not as sharp as that of flow around cube (shown in Ref. [1]). This implies that the wake area in which the flow recovers the momentum is larger than that for a cube placed normal to the flow. The velocity vectors change sign, but they show two distinct recovery regions in the wake for  $Re \geq 784$ . Unlike flow around a cube, the gain in momentum happens with two peaks of recovered velocity vectors after the recirculation region.

The wake has two distinct regions: the recirculation region and the postrecirculation region. The axial distance along the centerline at which the streamwise velocity changes its sign is defined as the recirculation length. Figure 7 shows the change in the direction of velocity vectors in the wake. The recirculation length for both the cube and the oriented cube increases between  $Re = 533$  and  $Re = 784$ ; then there is a sharp drop in the recirculation length of the cube (Fig. 8). The recirculation

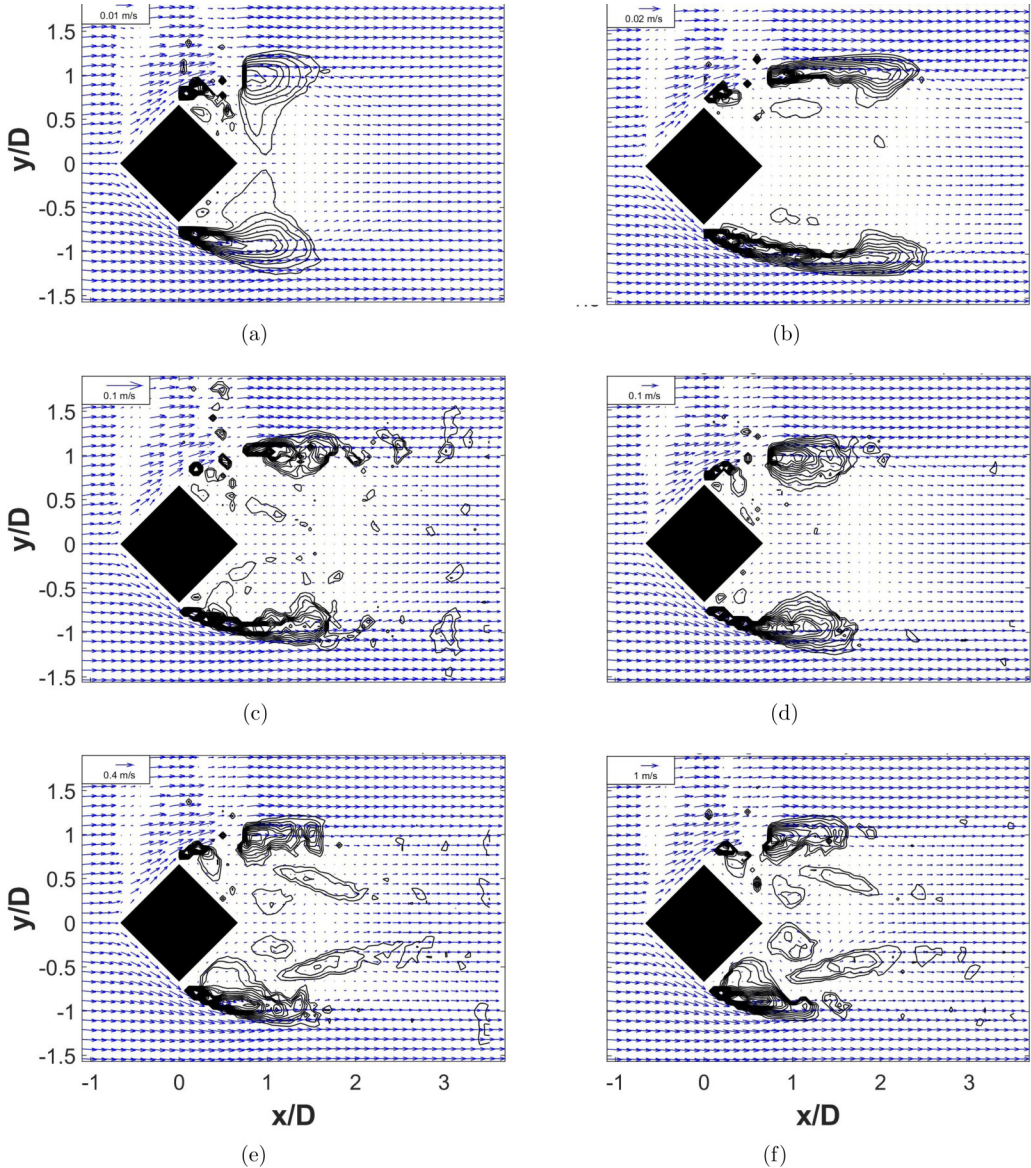


FIG. 7. Time-averaged streamwise velocity vectors at various Reynolds numbers and contours of vortices identified using swirling strengths: (a)  $Re = 533$ , (b)  $Re = 784$ , (c)  $Re = 2200$ , (d)  $Re = 5300$ , (e)  $Re = 18620$ , and (f)  $Re = 46800$ .

length for  $Re \leq 784$  is lesser for oriented cube and at all higher  $Re$  the magnitude is greater than the length for flow around a cube. The recirculation length increases with  $Re$  at lower Reynolds numbers due to the dominant effect of viscous diffusion [6,24] which influences the flow separation. At higher  $Re$  (greater than 784), the effect of viscosity decreases and flow separates at a wider angle and travels a larger distance for an oriented cube as compared to the flow separated at the leading edge of the cube. The recirculation lengths for a cube varies within a range of 25% of the cube dimension for  $Re > 1200$ , whereas for an oriented cube the range is 30% of the cube dimension at higher Reynolds numbers.

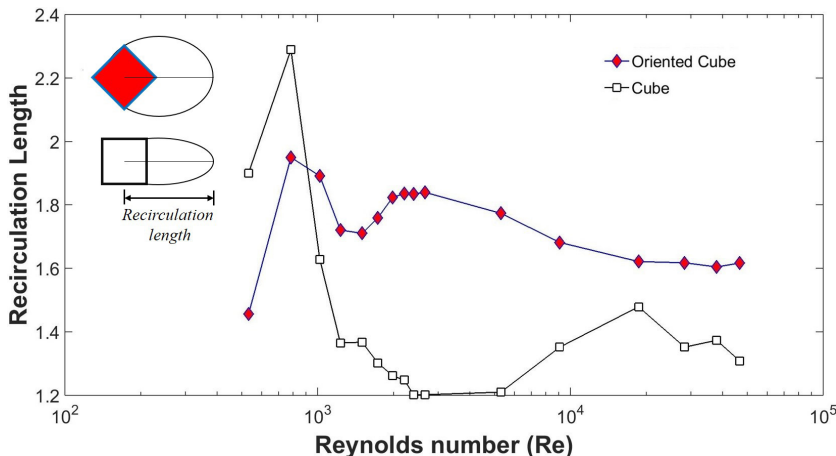


FIG. 8. Variation of recirculation length with Reynolds numbers for a cube and an oriented cube.

A symmetry is observed at  $Re = 784$  with two similar lobes of the deficit zone around the centerline of the wake for the oriented cube. This symmetry around the centerline is lost at higher  $Re$ . Ensemble averages taken over the entire data set show asymmetry for the wake at lower  $Re$ , but when a smaller ensemble is used a symmetric mean field is obtained. Since the images for PIV measurements are taken at 1 Hz, we believe that this loss in symmetry might be due to the captured phases in the overall data set which might not necessarily be integral multiples of 1 s. In addition, the presence of many smaller eddies in the wake contributes to the phased nature of the mean velocity field. So average velocity fields at certain  $Re$  show small asymmetries for a few cases and not for others. Asymmetry in the wake is persistent at higher-Reynolds-number flows due to the higher rate of shedding in the flow with many smaller eddies. This is appreciated when one looks at the vortical structures in the mean vorticity field, identified using the swirling strength as shown in Fig. 7.

The swirling strength (first introduced by Zhou *et al.* [40]) was used to identify the vortical structures in the flow using the eigenvalues of the velocity gradient tensors. The imaginary eigenvalue  $\lambda_{ci}$  represents the strength of the local swirling motion. Adrian *et al.* [41] proposed the use of the two-dimensional velocity gradient tensor  $\mathbf{J}$  defined as

$$\mathbf{J} = \begin{bmatrix} \frac{\partial u}{\partial x} & \frac{\partial u}{\partial y} \\ \frac{\partial v}{\partial x} & \frac{\partial v}{\partial y} \end{bmatrix}, \quad (7)$$

where  $x$  and  $y$  are directions and  $u$  and  $v$  are velocities. The eigenvalues of  $\mathbf{J}$  are estimated and the vorticity is identified as the isoregions of  $\lambda_{ci} > 0$ .

The superimposed swirling strength (isoregions of  $\lambda_{ci} > 0$ ) in Fig. 7 shows the nature of the vortex in the wake. Since the flow is three dimensional the identified vortex structures at various Reynolds numbers help elucidate the behavior of the wake. The identified swirling core at  $Re = 533$  is a thicker blob, but this is stretched at  $Re = 784$ . The stretching is expected due to the increased inertia in the flow. The vortex gets sheared by the flow and is stretched. This process of stretch and tilt breaks the vortices at higher  $Re$  (greater than 784), leading to a wake filled with smaller vortical structures. Many smaller vortices are seen all over the wake for  $Re > 18000$ . Khan *et al.* [24] discussed the fluctuating field for  $Re > 770$  for flow around a cube. The flow becomes chaotic due to breaking of larger vortices in smaller ones at higher  $Re$ . Smaller vortical structures for near wall flow at higher  $Re$  were identified by Khan *et al.* [42].

As seen above, the vorticity decays due to the breakdown and dissipation of larger vortices into smaller ones as one moves downstream in the wake. In order to quantify it, we plot the magnitude of normalized vorticity. Figure 9 shows the variation of clockwise and counterclockwise vorticity with

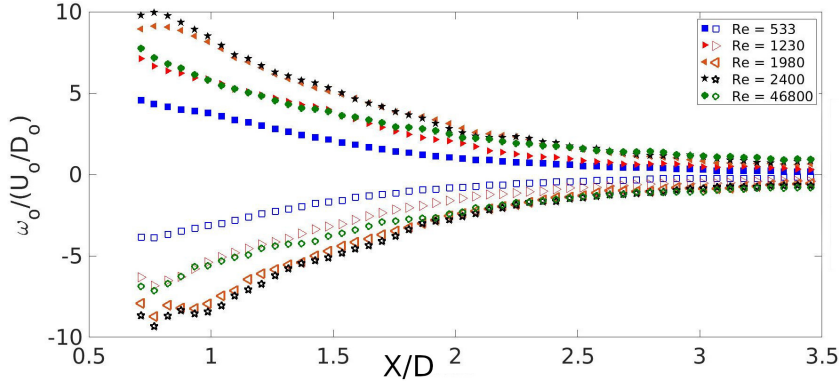


FIG. 9. Maximum vorticity at different axial distances from the oriented cube at various Re. Open markers represents counterclockwise vorticity and closed markers represents clockwise vorticity.

$x/D$ . The near wake shows a larger vorticity magnitude at  $Re = 2400$  as compared to  $Re = 46800$ . The magnitude is lowest for  $Re = 533$ .

### C. Velocity profiles in the wake

The time-averaged velocity in the wake is presented in this section to understand the kinematics of the wake. The velocities are presented for flow around an oriented cube at various axial locations. These velocities are normalized using the freestream velocity in the tunnel. The axial distances and transverse distances are normalized using the cube dimension  $D$ . The axial locations chosen are  $x/D = 1, 1.5, 2, 2.5,$  and  $3$ . Except for  $Re = 533$  and  $784$ , all other Re have a recirculation length less than  $2D$ . So the axial locations presented here cover both regions, within the recirculation zone and outside it.

#### 1. Variation with axial locations

Normalized streamwise velocities at various axial locations for different Reynolds number are presented in Fig. 10. The streamwise velocity contour for an oriented cube has comparatively flatter profiles for  $Re = 533$ . A shorter recirculation region with a wider wake width creates a flat profiled recirculation region as observed from Fig. 7. The velocity profiles for  $Re = 533$  have single peaks (Fig. 10). There is a rapid gain of around 18% in the streamwise velocity component between  $x/D = 1.5$  and  $x/D = 2$ . After  $x/D = 2$  the rate of gain in velocity is reduced, but asymmetry is noted in the velocity profile. At  $Re = 784$  the axial locations  $x/D = 1$  and  $1.5$  fall within the recirculation region and they have similar velocity deficits. At axial locations of  $x/D = 2$  and higher, two peaks are observed; the central region is accelerated relative to the outer wake region. The variation in the streamwise profile in the  $y$  direction at various axial locations is an indication of the three dimensionality in the flow. Streamwise velocity profiles at various axial locations show that the central portion has higher velocity. At higher Re (greater than or equal to 5300) the peaks become less dominant. The gain between  $x/D = 1.5$  and  $2$  is more than 25%. At higher Re multiple peaks are observed at  $x/D = 1.5$ . This axial location is within the recirculation region (Fig. 12). Moving beyond the recirculation region, for  $x/D \geq 2$  the streamwise velocity profile has two asymmetric peaks due to longer shear layers and the notable presence of transverse velocity components. The wake for an oriented cube is noticeably different from that of a cube [1]. The wake of the cube has a single peak at all  $Re \in (500, 55000)$ . Both the cube and the oriented cube have a maximum velocity deficit at  $Re = 784$ . The trend shown by the maximum velocity deficit is a characteristic of the wake behavior at various Reynolds numbers.

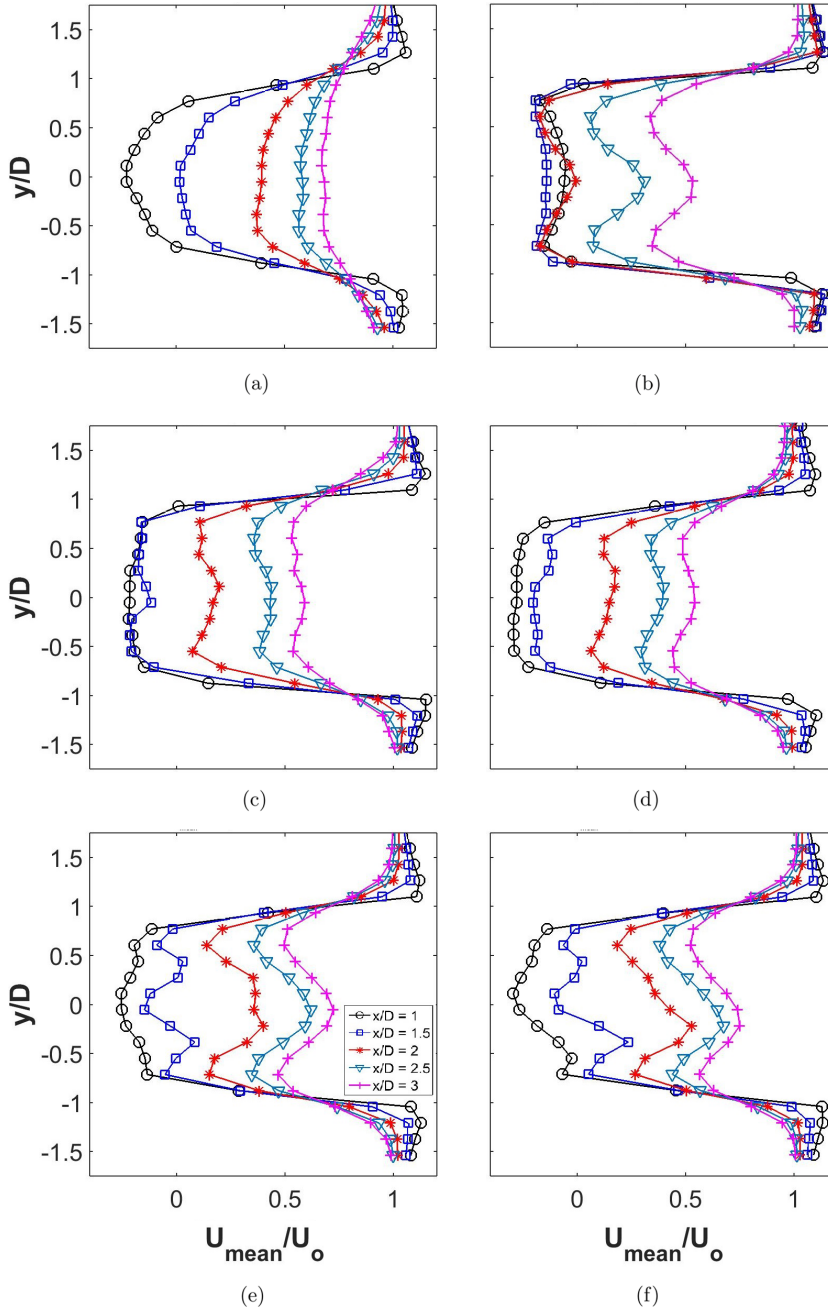


FIG. 10. Time-averaged normalized streamwise velocity at various axial locations for different Reynolds numbers: (a)  $Re = 533$ , (b)  $Re = 784$ , (c)  $Re = 2200$ , (d)  $Re = 5300$ , (e)  $Re = 18620$ , and (f)  $Re = 46800$ .

Figure 11 shows the variation of the minimum of the streamwise velocity (i.e., maximum velocity deficit) at different axial locations in the wake of an oriented cube at various Reynolds numbers. Based on the maximum velocity deficit at different axial locations, six  $Re$  bands (A, B, C, D, E, and F) are noted with the deficit profile with respect to  $Re$  as shown in Fig. 11. Using the variation of

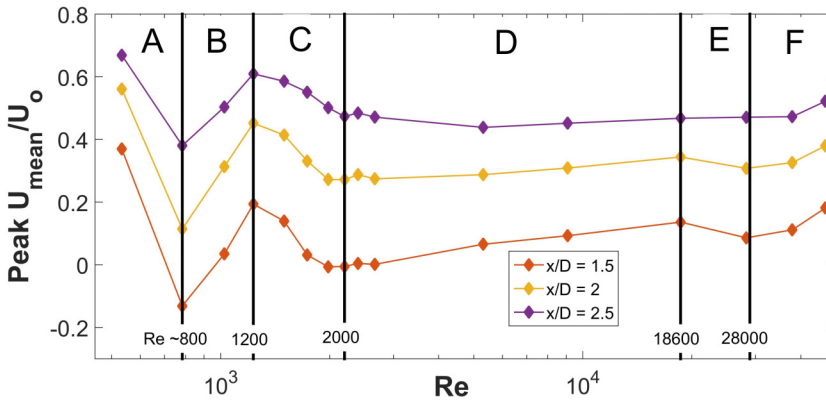


FIG. 11. Velocity deficit peak for different axial locations at various Reynolds numbers.

the maximum velocity deficit at various axial locations for different Reynolds numbers, transitions in the slopes are noted. The identified values are around  $Re = 800$ ,  $1200$ ,  $2000$ ,  $18600$ , and  $28000$ . This minimum velocity is the deficit peak of the streamwise velocity profile at any axial location. The profile at different axial locations for all  $Re$  follows a similar trend: The deficit decreases further from  $Re = 533$  to  $Re = 784$ . There is a gain noted between  $Re = 800$  and  $1200$ . After  $Re = 1200$ , the value of the velocity deficit decreases until  $Re = 2600$ . The velocity profile then has a very slow increase until  $Re = 18600$  and then another small dip is noted at  $Re = 28000$ . These profiles explain the trend in velocity deficit at various Reynolds numbers. These are the direct outcome of the momentum exchange in the wake and are associated with the drag forces. The nature of the profiles gives an impression of probable transition points at  $Re \sim 800$ ,  $1200$ ,  $2000$ ,  $18600$ , and  $28000$ . It should be noted that bands A and B are only rough estimates due to fewer data points below  $Re \leq 1200$ .

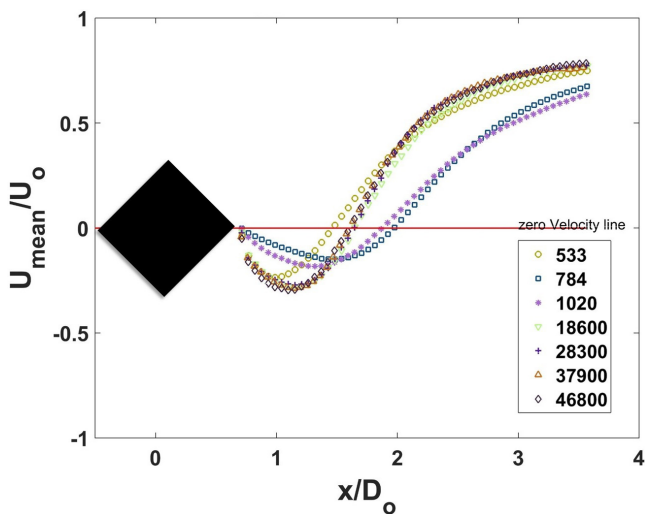


FIG. 12. Variation of normalized time-averaged velocity at the centerline.

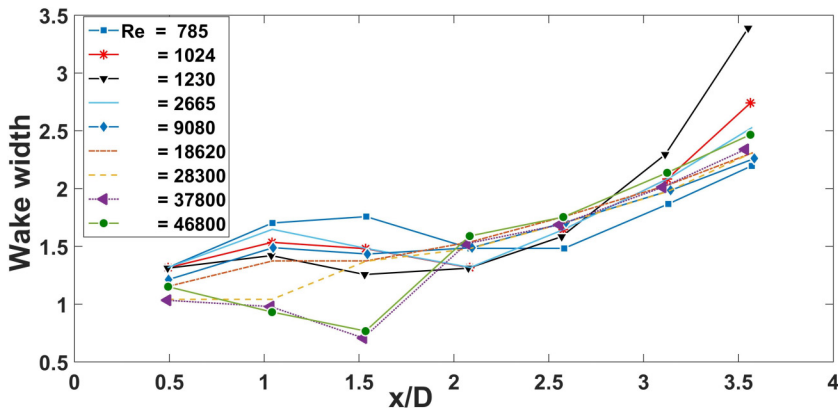


FIG. 13. Wake width at various axial locations for different Reynolds numbers.

## 2. Variation of velocity at the centerline and wake width

The centerline velocity profiles for the wake give an idea about the size of the wake and the rate and nature of velocity recovery with respect to the axial distance in the wake. Figure 12 shows the centerline streamwise velocity profile at various Reynolds number. The velocities at higher Re converge within a narrower band compared to that around a cube [1]. The gain in centerline velocity is 78% of the freestream velocity at  $x/D = 3.2$ . At higher Re there is a rapid gain as compared to that of a cube placed normal to the flow. The gain in the streamwise velocity component at higher Re is from 59% to 75% between  $x/D = 2.5$  and 3.2. At higher Re (greater than 18 000) and  $x/D = 2.5$  the velocity is in a band of 5%. This rapid gain in the centerline velocity hints at better mixing for flow around an oriented cube. Most of the changes in the velocity flow pattern happen within an axial location of  $x/D = 2$ , which is roughly the wake length (the axial distance along the centerline after which the velocity changes direction). Beyond  $x/D = 2$ , velocity profiles collapse for  $Re = 784$  and 1020. Similarly, the profiles collapse to a single value at higher Re (greater than 1020). A trend similar to the wake length is noted for the wake width too (Fig. 13).

Figure 13 shows the wake width at various axial locations for different Reynolds numbers. The wake width is estimated as the transverse distance from the center of the wake where 50% of the deficit is recovered. Since the centerline velocity is also recovered farther away from the body, the velocity gradient is less steep in the transverse direction at these locations. Therefore, the transverse length required to recover the 50% of the deficit increases with axial distance. The near wake width (for  $x/D < 2$ ) at higher Re is lesser compared to those at lower Re. This is due to the inertia at higher Re which washes the separated shear layer farther downstream before it can exchange velocity in the transverse direction and grow. At higher Re the wake width becomes independent of Re because the residence time for the separated shear layer is reduced and vortices are convected downstream. Similar behavior was noted for flow around a cube [1].

Fixed separation points for flow around a cube make it distinct from spherical or circular bluff bodies with the separation point dependent on Re. The orientation of the cube gives different trajectories to the shear layers formed after the flow separation happens at the fixed corners. The wake width for an oriented cube is greater than  $\sqrt{2}D$ . The shear layers for a cube interact in the wake but for an oriented cube they roll up in small vortices which are shed in the wake.

## D. Streamwise variation in turbulence statistics

The wake of an oriented cube in the investigated range of Reynolds numbers is turbulent. An understanding of the fluctuating velocity field is necessary to comprehend the wake behavior. The following sections examine the normalized root mean square velocities and Reynolds shear stress.

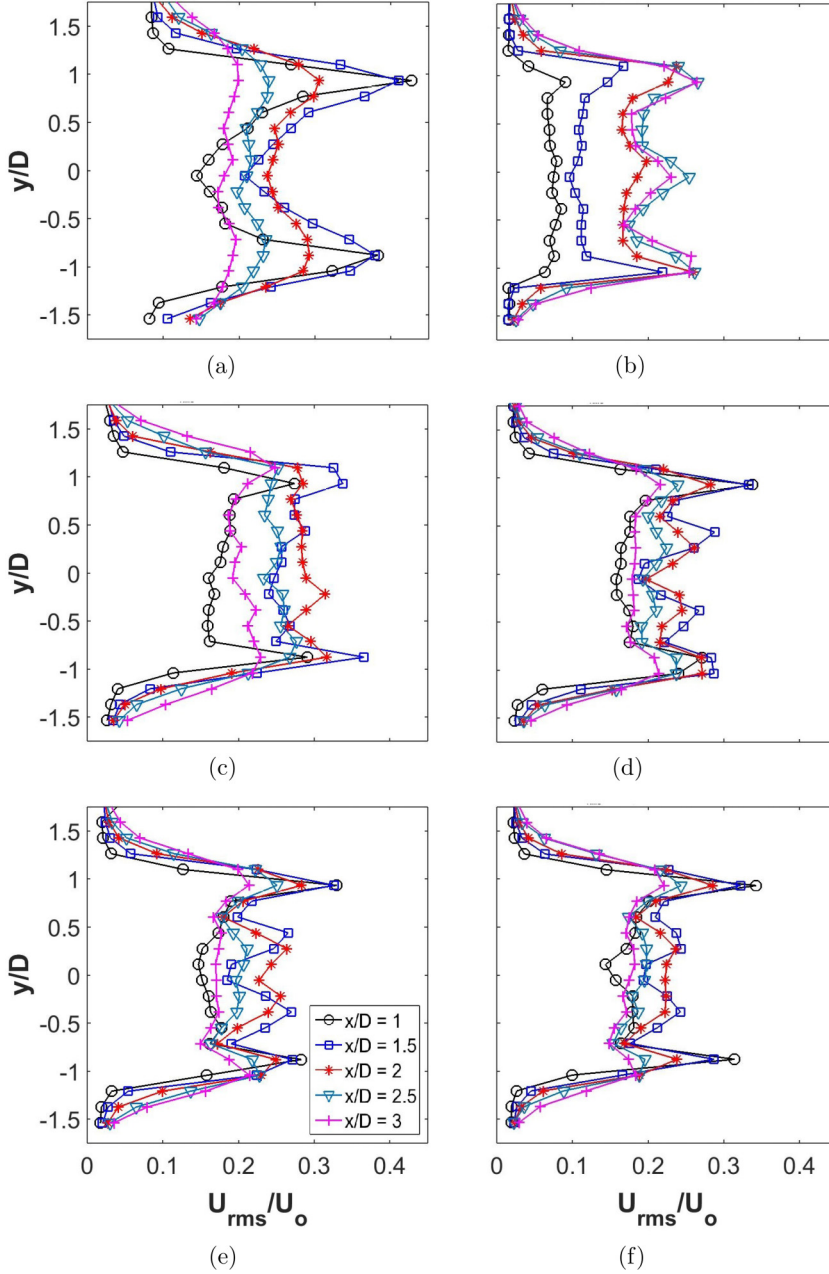


FIG. 14. Normalized  $U_{rms}$  at various axial locations for different Reynolds numbers: (a)  $Re = 533$ , (b)  $Re = 784$ , (c)  $Re = 2200$ , (d)  $Re = 5300$ , (e)  $Re = 18620$ , and (f)  $Re = 46800$ .

### 1. Normalized root mean square velocity profiles

Root mean square velocities are normalized with the freestream velocity and plotted at different axial locations to get an idea about the temporal effect of the fluctuations in the flow. Figures 14 and 15 show the normalized rms velocities for both the streamwise ( $U_{rms}$ ) and transverse ( $V_{rms}$ ) velocity components.

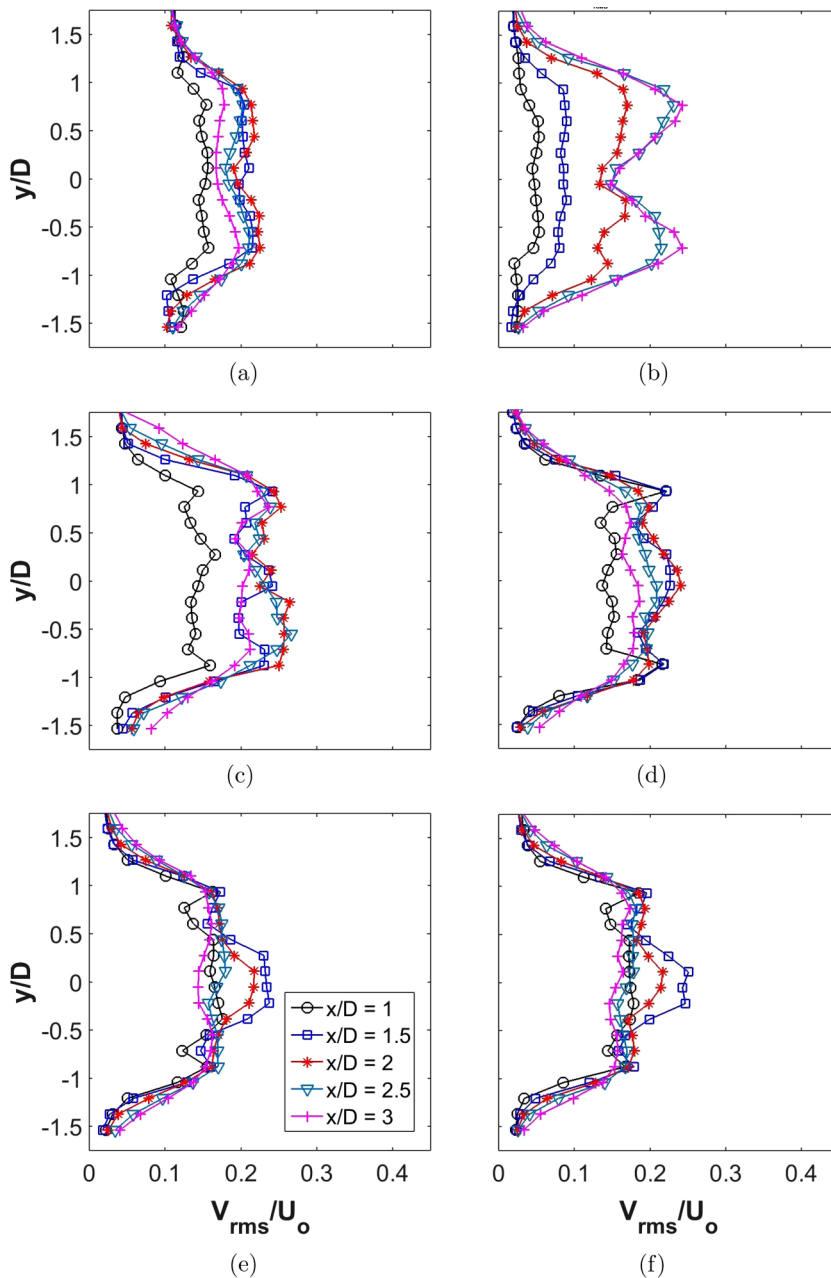


FIG. 15. Normalized  $V_{rms}$  at various axial locations for different Reynolds numbers: (a)  $Re = 533$ , (b)  $Re = 784$ , (c)  $Re = 2200$ , (d)  $Re = 5300$ , (e)  $Re = 18620$ , and (f)  $Re = 46800$ .

Normalized  $U_{rms}$  profiles for flow around a cube have two peaks [1] due to the presence of shear layers. At any  $Re$ , the  $U_{rms}$  decreases as one moves in the axial direction away from the cube since the shear layers weaken and the fluctuations are absorbed in the momentum exchange with the freestream velocity. The turbulent action is predominant in the near wake of the cube and it weakens farther away from the bluff body.

For flow around an oriented cube the  $U_{\text{rms}}$  action is noted in four different categories: (i) the magnitude of the rms velocity, (ii) the transverse stretch in  $y/D$ , i.e., width of the velocity profile at any axial location, (iii) the behavior of the rms in the axial direction, and (iv) the number of peaks in the rms velocity profiles at various axial locations in the wake. The magnitude of  $U_{\text{rms}}$  is greater than those for flow around a cube at various  $x/D$  and Reynolds numbers. The rms velocity stretch in the transverse direction is greater owing to the obstructing cross section along with the wider wake which was observed in the swirling strength isoregions velocity vector plots (Fig. 7). Along axial locations the average value of  $U_{\text{rms}}$  at  $x/D = 1$  is lower for all Re since this location lies within the recirculation region. At higher axial locations for  $x/D \geq 1.5$ , we notice two or more peaks. Multiple peaks indicate the presence of shear layers and their breakdown into many smaller vortices which create packets of fluctuating components in the wake. These multiple peaks are limited until  $x/D \leq 2$  and then a flatter profile with a maximum of two peaks is observed. This flattening is due to the exchange of momentum between the freestream and the wake. The two weak peaks are remnants of the shear layer, which is carried downstream in the far wake by the streamwise flow component.

Normalized  $V_{\text{rms}}$  profiles are shown in Fig. 15 at different axial locations and Reynolds numbers. These profiles for flow around an oriented cube are wider than that for flow around a cube [1]. At Re = 533 two peaks are present at  $x/D$  greater than  $1.5D$ . At Re = 784 double peaks develop at  $x/D = 2.5$  and 3, before which the flatter  $V_{\text{rms}}$  profiles depict lesser transverse momentum exchange. The  $U_{\text{rms}}$  profiles of Fig. 14 show the presence of multiple peaks at higher Re, to which is added the presence of transverse fluctuations as shown in Fig. 15. The central portion of the rms profiles in the range from  $y/D = -0.5$  to  $0.5$  peaks at  $x/D = 1.5$ , where the  $U_{\text{rms}}$  has a local minimum. The effect of the shear layer is more dominant in the  $U_{\text{rms}}$  profiles since the flow is in the streamwise direction and the shear layer also moves in the same direction.

The ratio of  $U_{\text{rms}}$  and  $V_{\text{rms}}$  (not shown) gives an estimate of the equivalence of the fluctuating components in the flow. At Re = 533 and 784 the flow has directional fluctuations with  $U_{\text{rms}}/V_{\text{rms}}$  profiles showing larger peaks at  $x/D = 1$  and  $1.5$ , which are axial locations within the recirculation region. The streamwise component of the rms is dominant for the normal cube as compared to that of an oriented cube. Beyond the recirculation region, lower peaks are noted. At higher Re, the dominant peaks are washed away due to many smaller vortices. This shifts the flow towards being more isotropic, hinting at enhanced transverse fluctuations. The width of the wake with isotropic flow, i.e.,  $U_{\text{rms}} \sim V_{\text{rms}}$ , is larger and prevalent for an oriented cube. This indicates more homogenizing and a better mixing ability of an oriented cube as compared to a cube placed normal to the flow.

## 2. Reynolds shear stress

The turbulent wake behavior for advection is understood using the Reynolds shear stress (RSS). Figure 16 shows the RSS profiles at various axial locations at different Reynolds numbers for flow around an oriented cube. The RSS profiles are symmetric about the centerline with one half showing a positive flux and the other showing negative flux for flow around a cube. At the axial locations  $x/D = 1$  and  $1.5$  at Re = 784 the profiles are flatter and two opposite-sign peaks appear at higher  $x/D$ . These peaks explain the transverse momentum exchange due to  $v'$ . The flow around an oriented cube has RSS profiles with peaks at larger  $y/D$ , which is expected due to a wider wake as compared to a cube placed normal to the flow. The presence of many smaller vortices in the near wake and larger recirculation lengths explains the relative irregularity in the RSS profiles. The magnitude of advection is larger than that of a normal cube. For all higher Re the RSS profiles are flatter with multiple peaks. Many small eddies are created in the wake but most of them are washed in the streamwise direction. A wider wake with a longer recirculation region ( $x/D \sim 2$ ) along with flatter streamwise wake as shown in Fig. 7 is the reason for such RSS profiles at all axial locations and all higher Re.

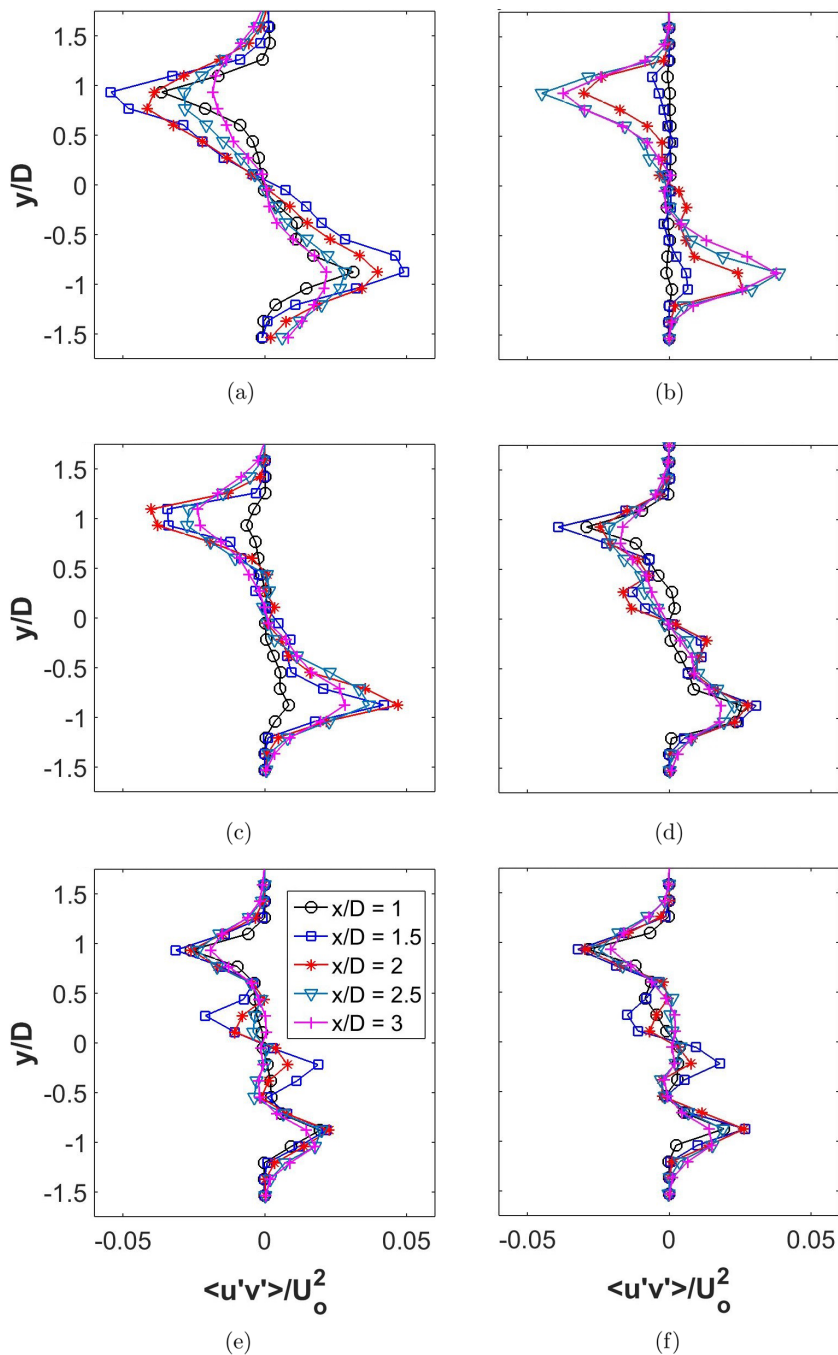


FIG. 16. Reynolds shear stress at various axial locations for different Reynolds numbers: (a)  $Re = 533$ , (b)  $Re = 784$ , (c)  $Re = 2200$ , (d)  $Re = 5300$ , (e)  $Re = 18620$ , and (f)  $Re = 46800$ .

### E. Insights from proper orthogonal decomposition

Proper orthogonal decomposition (briefly explained in Sec. II C) was used to investigate the wake of the oriented cube. This process helped identify coherent structures by separating modes based on

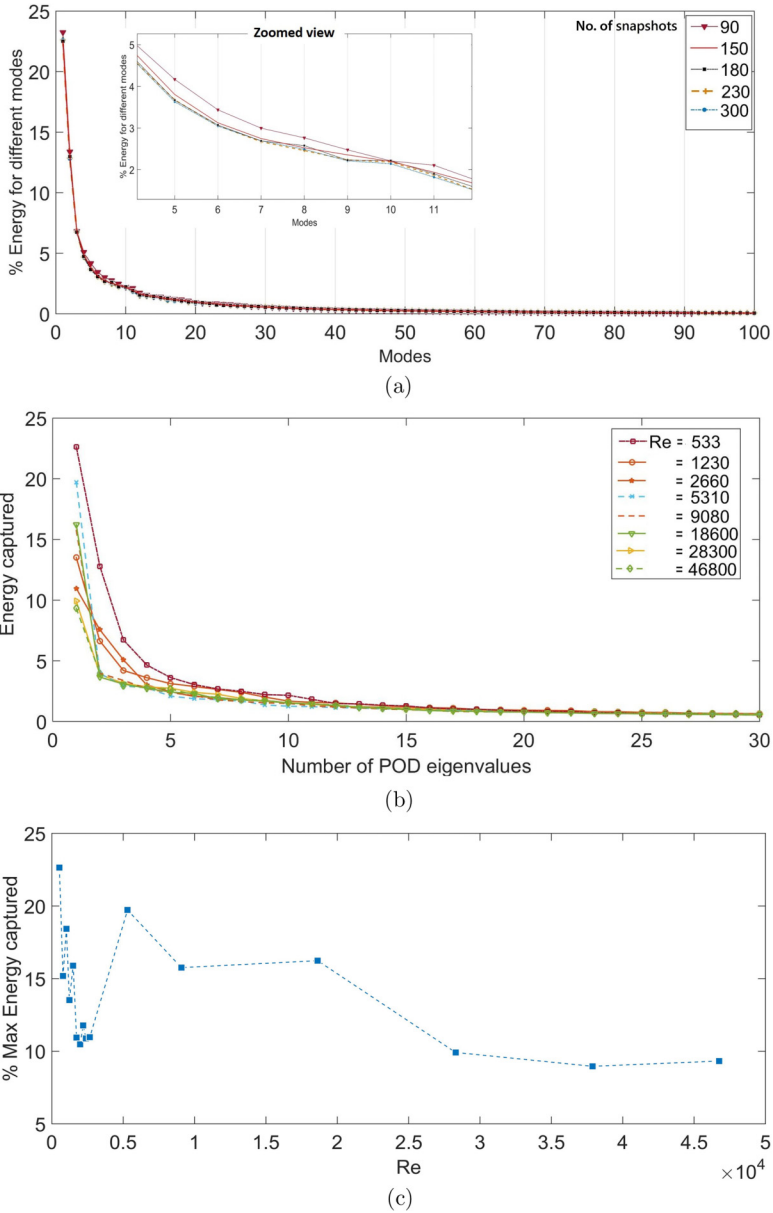


FIG. 17. Energy fraction (percent energy) for different modes estimated using eigenvalues. (a) Snapshot independence test done at  $Re = 533$  showing the number of snapshots greater than 230 converging to the percentage of the energy distribution across various modes, (b) percentage of energy captured for different modes at various  $Re$ , and (c) percentage of energy captured for the first mode at different Reynolds numbers.

turbulent kinetic energy. Decomposition of the flow domain into different modes helps in choosing modes which have higher energy content and which contribute to the coherent structures. Coherent structures evolve over time and space. In addition, the obtained POD coefficients help explain the turbulent kinetic energy in the wake at various Reynolds numbers.

A snapshot independence test was done using 90, 150, 180, 230, and 300 image frames. The percentage of energy content for each mode using different sets of image frames as snaps is shown

in Fig. 17(a). It was found that beyond 230 the highest share of the energy fraction is almost the same. The inset in Fig. 17(a) shows how the energy distribution collapses for different sets of snaps more than 230 for higher modes.

### 1. Interpretation of energy content in the flow

The energy content of different modes for flow around an oriented cube is shown in Fig. 17(b). The highest energy of 22.64% for the first mode is for  $Re = 533$ . The share of energy for different modes asymptote at the 20th mode, after which modes have a negligible share of energy (below 0.7%). The energy share for all Reynolds numbers falls within 2–3.5 % for modes greater than 6. Figure 17(c) shows the percentage of energy in the first mode at various  $Re$ . Here  $Re = 5300$  is an interesting aberration for mode 1 with a local maximum of 19.72% for an oriented cube [Fig. 17(c)]. All the modes converge to energy less than 1% after the 15th mode. The change in nature of the profile in Fig. 17(c) correlates with the Reynolds numbers noted as critical points in Fig. 11. The POD coefficients further help elucidate the energy content of each mode over a cycle. At higher  $Re$ , the total energy is distributed over many modes due to energy cascading into smaller eddies present in the decomposed flow field of higher modes. This causes the first mode for a fluctuating velocity field to have a lower share of the total energy content for flow at higher  $Re$ .

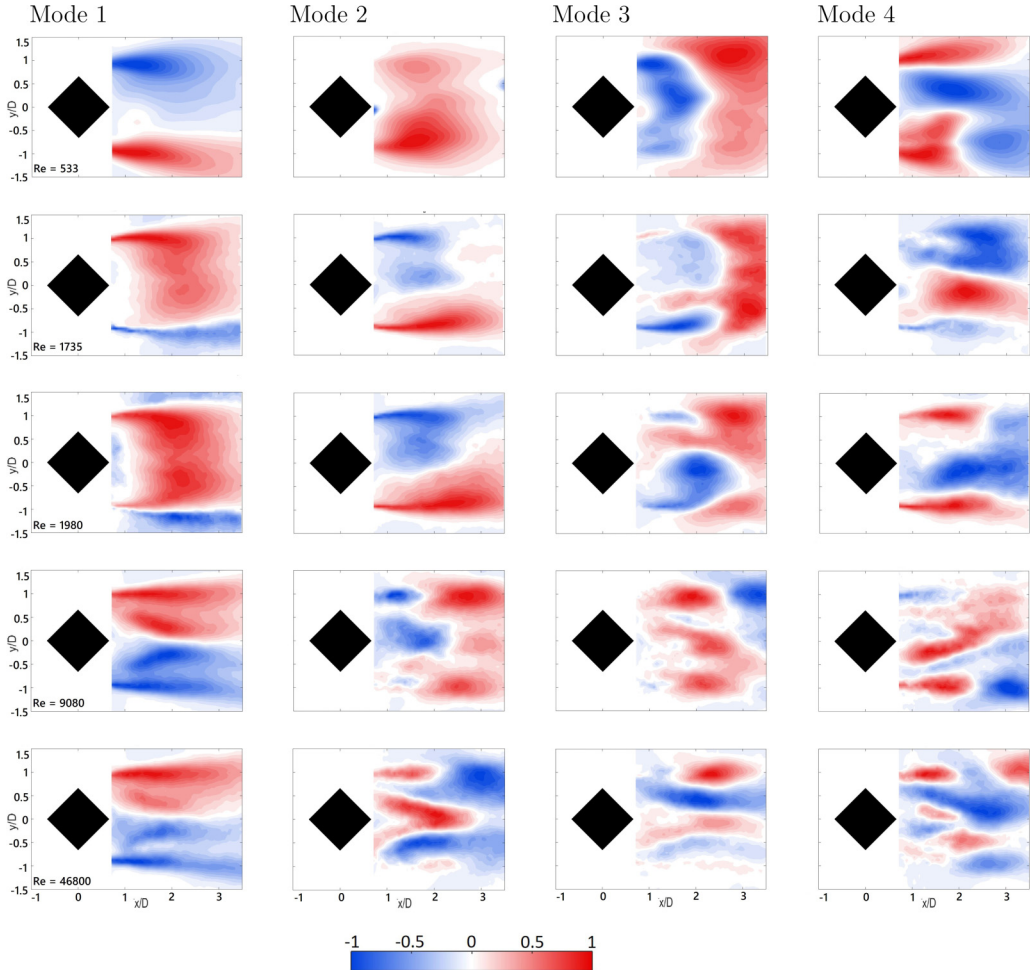
Figure 17(b) explains the energy content (using eigenvalues) for various modes. Coherent structures associated with different modes containing different energy fractions will help us understand the flow behavior. The following section explains the flow structure for different modes.

### 2. Flow structure for different modes

Proper orthogonal decomposition done over instantaneous velocity fields decomposes various modes. Since the coherent structures are dictated by the fluctuating component of velocity field, decomposition is performed on the fluctuating velocity fields estimated after subtracting the mean velocity field from the instantaneous velocity fields. Figures 18 and 19 show the streamwise flow structures for the first four modes (1, 2, 3, and 4) at various Reynolds numbers and the phase dependence of POD time coefficients. The POD time coefficients represent the temporal behavior of the flow in a particular mode. The POD time coefficients, when visualized along with the flow structure of the mode, help us understand mode-based growth of coherent structures.

The fluctuations in  $u'$  for mode 1 indicate the presence of shear layers (Fig. 18). The decomposed  $u'$  for  $Re = 533$  and 1735 are not symmetric, but at higher  $Re$  symmetry is restored for the two directions of fluctuations. The rear side of the oriented cube shows opposite-sign fluctuations at  $Re = 5300$  (although a weaker pattern is noted at  $Re = 2400$  too). The growing asymmetry with Reynolds number disappears at higher  $Re$  since the inertia dominates the flow and we note a Reynolds number independence at higher  $Re$ . A similar observation was noted for flow around a cube at higher  $Re$  [1]. The similarity in the flow patterns of the first mode for  $Re = 1735$  and 1980 emphasizes the earlier proposition of possible regime between  $Re = 1200$  and 2000 (shown in Fig. 11). Bigger structures for mode 1 hint at the larger energy content of the first mode (Fig. 18). The size of the structures decreases at higher  $Re$ . For  $Re = 1735$  and 1980 mode 2 has two big lobes (of a denser velocity region) in the wake. We notice that these lobes are complementary to the pattern in mode 1 for these two Reynolds numbers. At all higher  $Re$ , these structures are smaller for mode 2. The sizes become smaller for higher modes at all Reynolds numbers. Higher modes have an irregular distribution of  $u'$  with noticeable action in the near wake. Similar breaking of planar symmetry for higher modes at  $Re = 3000$  for flow around a disk was reported by Yang *et al.* [43] using three-dimensional POD.

Reconstruction of  $u'$  for each mode is done using the orthogonal basis function and POD time coefficients as mentioned in Eq. (3). Figure 19 shows the time coefficient phase plots to ascertain the role of each time coefficient over a cycle in the reconstruction of the mode. This helps in figuring out how in-phase or out-of-phase time coefficients contribute to the growth or distortion of structures generated using the summation of modes. The normalized time coefficients  $c_1/\lambda_1^{1/2}$  vs  $c_2/\lambda_2^{1/2}$


 FIG. 18. Four different modes of  $u'$  at various Re.

and  $c_3/\lambda_3^{1/2}$  vs  $c_4/\lambda_4^{1/2}$  have been plotted for modes 1, 2, 3, and 4. The coefficients  $c_1/\lambda_1^{1/2}$  and  $c_2/\lambda_2^{1/2}$  are highly uncorrelated for  $Re = 533$  [Fig. 19(a)]. The coefficients are relatively correlated for modes 3 and 4. This is evident from the contours of the streamwise fluctuating component as well (Fig. 18). Mode 1 has shearing regions, whereas mode 2 is only directed in the streamwise direction. Modes 3 and 4 have regions whose structures overlap and would help in the growth of reconstructed structures. Table III gives the percentage energy distribution in each mode.

The POD coefficients  $c_1/\lambda_1^{1/2}$  and  $c_2/\lambda_2^{1/2}$  are out of phase but are correlated for  $Re = 1735$  [Fig. 19(b)] within a radius of 40. The radii are drawn as limit circles enclosing the scatter plot of POD coefficients. Yang *et al.* [43] used limit circles for scatter plots of POD coefficients to categorize vortex shedding modes. The coefficients  $c_3/\lambda_3^{1/2}$  and  $c_4/\lambda_4^{1/2}$  are spread until a radius of 60. The zone between  $r = 40$  and 60 shows a higher influence of modes 3 and 4, which are well correlated in the inner radius of 40 too. Although the percentage of energy content in modes 3 and 4 is lower, we note the directionally similar regions in modes 2, 3, and 4 that help in their constructive superposition to form a coherent structure. This is also indicated by the uniform scatter of coefficients in the limit circles.

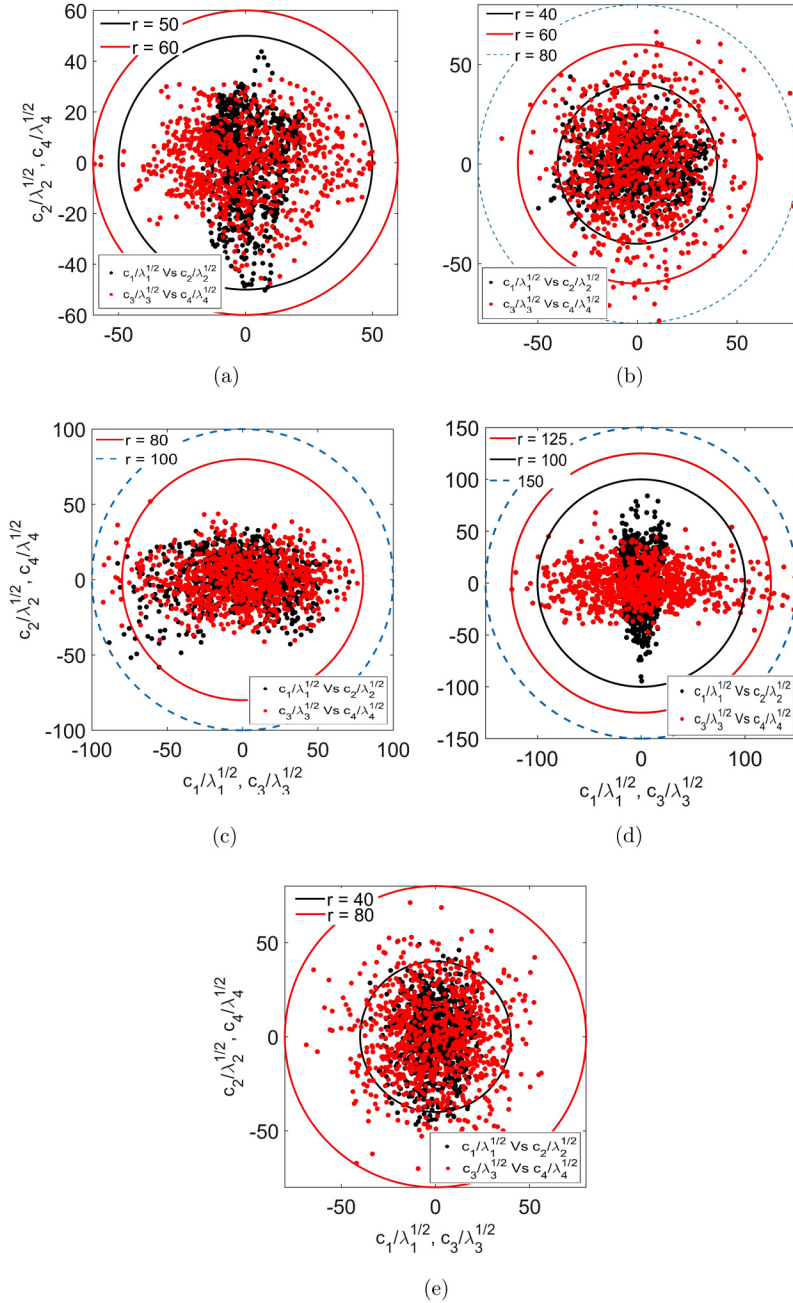


FIG. 19. Scatter plot for POD coefficients for modes 1, 2, 3, and 4 at various Re: (a) Re = 533, (b) Re = 1735, (c) Re = 1980, (d) Re = 9080, and (e) Re = 46800.

Figure 19(c) shows an elliptic distribution of the coefficients. It is observed that the amplitudes of  $c_1/\lambda_1^{1/2}$  and  $c_3/\lambda_3^{1/2}$  are larger as compared to the other two coefficients. The structures of the modes and phases of the POD time coefficients indicate the formation of smaller coherent structures, when the modes will be superimposed for reconstruction of the field. The energy content for the first two

TABLE III. Percentage of energy content in various modes for Fig. 18.

Reynolds number	Energy (%)			
	Mode 1	Mode 2	Mode 3	Mode 4
533	22.64	12.79	6.72	4.65
1735	10.93	7.74	4.36	3.75
1980	10.48	7.04	4.53	3.22
9080	15.75	3.96	3.38	2.70
46800	9.32	3.95	2.92	2.77

modes is double the energy content of modes 3 and 4. The amplitudes of  $c_2/\lambda_2^{1/2}$  and  $c_3/\lambda_3^{1/2}$  are larger as compared to the other coefficients at  $Re = 9080$  [Fig. 19(d)]. The distribution of the two cases  $c_1/\lambda_1^{1/2}$  vs  $c_2/\lambda_2^{1/2}$  and  $c_3/\lambda_3^{1/2}$  vs  $c_4/\lambda_4^{1/2}$  is elliptic with major axes at an angle of 90°. There are regions of no overlap for the scatter plots due to the mode 1–mode 2 and mode 3–mode 4 time coefficients. The behavior of coefficients explains the formation of smaller coherent structures on the summation of these modes. This can also be appreciated by adding the first four modes of Fig. 18 at  $Re = 9080$ .

Table III shows that modes 2 and 3 have similar energy content. At higher Reynolds numbers the limit circle for the scatter of coefficients asymptotes to the one shown for  $Re = 46\,800$  in Fig. 19(e). The time coefficients for mode 2 have higher amplitude, so all  $c_1/\lambda_1^{1/2}$  vs  $c_2/\lambda_2^{1/2}$  plots have elliptic patterns. In addition,  $c_3/\lambda_3^{1/2}$  and  $c_4/\lambda_4^{1/2}$  are well correlated with a limit circle of radius  $r$  between 60 and 80.

In summary, proper orthogonal decomposition has improved our understanding of the energy content in the flow and helps establish the evolution of coherent structures. Using POD, an idea of the energy content in various modes was established along with the variation of maximum energy, i.e., energy content in mode 1 with Reynolds number. In addition, POD helped identify how the wake changes with mode and how its structure at a particular mode changes with  $Re$ .

### F. Coefficient of drag $C_d$

A modified wake survey method was used to calculate the coefficient of drag for the experimental data as

$$C_d = \frac{2}{D} \int_l \left\{ \frac{U_{\text{mean}}}{U_\infty} \left( \frac{U_{\text{mean}}}{U_\infty} - 1 \right) + \epsilon \left( \frac{U_{\text{mean}}}{U_\infty} - 1 \right) + \left( \frac{U_{\text{rms}}}{U_\infty} \right)^2 - \left( \frac{V_{\text{rms}}}{U_\infty} \right)^2 + \frac{1}{2} \left( 1 - \frac{U_0^2}{U_\infty^2} \right) \right\} dl, \quad (8)$$

where  $D$  is the cube dimension for a cube and  $\sqrt{2}$  times the cube dimension for an oriented cube,  $U_\infty$  and  $U_0$  are upstream and downstream freestream velocities, respectively,  $\epsilon = 0.5(1 - \frac{U_0}{U_\infty})$ ,  $l$  is the perpendicular length across the wake, and  $dl$  is the differential length. An explanation for the choice of this method for estimating drag coefficients is provided in Ref. [1]. The wake survey method suffers a limitation when used with highly unsteady flows [44]. Bohl and Koochesfahani [45] suggested a modified wake survey method to account for the fluctuations, pressure deficit, and streamwise velocity changes in the wake. The estimate of  $C_d$  presented here can be used to benchmark and validate computational fluid dynamics results. Figure 20 shows the variation of  $C_d$  with  $Re$  for the configuration investigated here.

The wake shape and recirculation length affect the forces around the bluff body. Unlike the steady regime where  $C_d$  and the recirculation length are inversely related,  $C_d$  and recirculation lengths are independent at higher Reynolds number. The streamlining effect of the near wake recirculation region observed at lower Reynolds number is replaced by the inertial effect and the recirculation region is smaller at higher  $Re$ . The contribution of viscous force is lesser at higher  $Re$  and the

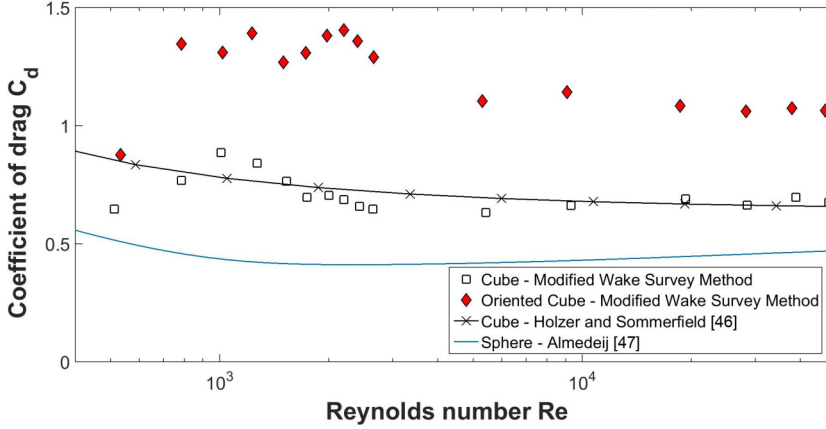


FIG. 20. Coefficient of drag for a cube and an oriented cube at various Reynolds numbers compared with correlations for a sphere and a cube.

projected obstacle area dominates the force dynamics around the body, i.e., form drag contributes more in the net drag around the body.

A cube can be considered as a special case of a square cylinder with an aspect ratio equal to 1. Dutta *et al.* [9] (working at  $Re = 410$ ) showed that for a lower aspect ratio (equal to 16) of the square cylinder  $C_d$  at an angle of incidence  $45^\circ$  is more than a  $0^\circ$  angle of incidence. The present case shows that an oriented cube, which is a cube placed at an angle of incidence of  $45^\circ$ , has  $C_d$  greater than that of a normal cube at all  $Re$ . Thus one can conjecture that the  $C_d$  for all lower aspect ratios is more for a  $45^\circ$  oriented square cylinder.

The estimated coefficients have been plotted along with Eqs. (9) [46] and (10) [47]. The drag coefficient for flow around a cube for  $Re < 10^6$  is given by

$$C_d = \frac{8}{Re} \frac{1}{\sqrt{\Phi_{\parallel}}} + \frac{16}{Re} \frac{1}{\sqrt{\Phi}} + \frac{3}{\sqrt{Re}} \frac{1}{\Phi^{3/4}} + 0.4210^{0.4(-\log\Phi)^{0.2}} \frac{1}{\Phi_{\perp}}, \quad (9)$$

where  $\Phi$ ,  $\Phi_{\parallel}$ , and  $\Phi_{\perp}$  are sphericity, cross-sectional sphericity, and longitudinal sphericity, respectively. The correlation of the drag coefficient for flow around a sphere in  $10 < Re < 10^6$  is

$$C_d = \left( \frac{1}{(\phi_1 + \phi_2)^{-1} + (\phi_3^{-1})} + \phi_4 \right)^{1/10}, \quad (10a)$$

with

$$\phi_1 = (24 Re^{-1})^{10} + (21 Re^{-0.67})^{10} + (4 Re^{-0.33})^{10} + (0.4)^{10}, \quad (10b)$$

$$\phi_2 = \frac{1}{(0.148 Re^{0.11})^{-10} + (0.5)^{-10}}, \quad (10c)$$

$$\phi_3 = (1.57 \times 10^8 Re^{-1.625})^{10}, \quad (10d)$$

$$\phi_4 = \frac{1}{(6 \times 10^{-17} Re^{2.63})^{-10} + (0.2)^{-10}}. \quad (10e)$$

Estimated values of drag coefficients for flow around a cube match closely with the correlation proposed by Hölzer and Sommerfeld [46]. The  $C_d$  for an oriented cube is larger than  $C_d$  for a cube which is larger than the  $C_d$  for the sphere obtained using correlation given by Almedej [47]. This shows that the bluffness of these three bodies decreases in the following order: oriented cube > cube > sphere for  $Re \in (500, 50000)$ .

#### IV. CONCLUSION

Flow around an oriented cube was investigated using two-dimensional particle image velocimetry measurements performed at 1 Hz. The present experimental investigation provided a detailed understanding of the wake of an oriented cube and compared it with a cube placed normal to the flow. The  $Re \in (500, 50\,000)$  investigated in the present work were in the unsteady regime.

The oriented cube shed smaller eddies in the wake. The number of recirculating zones in the wake increased with  $Re$  and the wake was distributed with many smaller recirculating zones for  $Re > 2660$ . The time-averaged streamwise velocity for flow around an oriented cube was flatter at  $Re = 533$  and had multiple peaks for  $Re \geq 784$ . Velocity vectors for flow around an oriented cube showed two lower peaks (trough) for velocities at all axial locations, while there was recovery of the velocity deficit. The recovery of velocity deficit was faster for an oriented cube due to the presence of many small eddies in the wake, which help achieve better diffusion and mixing. Centerline velocities showed that the gain in velocity is more for flow around an oriented cube, i.e., 78% as compared to 66% for flow around a cube at  $x/D = 3.2$ .

The transitions in the slopes for maximum velocity deficit at various  $Re$  were noted around  $Re = 800, 1200, 2000, 18\,600, \text{ and } 28\,000$ .

Reynolds shear stress had negative and positive peaks showing the transverse direction of momentum flux with wider wake. Normalized  $U_{\text{rms}}$  profiles have double peaks at  $Re = 533$  and multiple peaks at higher  $Re$ . Asymmetry was noted in the  $V_{\text{rms}}$  profiles at different axial locations. A flatter profile was noted in some cases ( $Re = 533$  and  $784$ ) at smaller axial locations followed by double or multiple peaks at larger axial locations. In addition,  $U_{\text{rms}} \sim V_{\text{rms}}$ , which is evidence of a homogenizing fluctuating field with a better mixing ability.

Proper orthogonal decomposition analysis of the fluctuating velocity field was used to extract different modes and examine the coherent structures associated with each mode. Energy fraction associated with each mode at a particular  $Re$  helped us understand the distribution of energy in the modes. The phase portraits of consecutive time coefficients along with structures of streamwise components for the first four modes helped elucidate the nature and evolution of coherent structures at various  $Re$ .

This work has presented experimental results for flow around an oriented cube and has reported a comparison with flow around a normal cube. Further work can be done to capture images at higher frequency for better time resolution. Three-dimensional measurements of flow around an oriented cube is an open area for detailed experimental investigation using three-dimensional PIV and/or simultaneous measurements in orthogonal planes.

#### ACKNOWLEDGMENT

The authors are grateful to Indian Institute of Technology (IIT) Bombay for providing some funds for this work.

- 
- [1] M. H. Khan, P. Sooraj, A. Sharma, and A. Agrawal, Flow around a cube for Reynolds numbers between 500 and 55,000, *Exp. Therm. Fluid Sci.* **93**, 257 (2018).
  - [2] S. Murakami and A. Mochida, On turbulent vortex shedding flow past 2D square cylinder predicted by CFD, *J. Wind Eng. Ind. Aerodyn.* **54**, 191 (1995).
  - [3] A. K. Saha, K. Muralidhar, and G. Biswas, Transition and chaos in two-dimensional flow past a square cylinder, *J. Eng. Mech.* **126**, 523 (2000).
  - [4] A. Sharma and V. Eswaran, Heat and fluid flow across a square cylinder in the two-dimensional laminar flow regime, *Numer. Heat Transfer A* **45**, 247 (2004).
  - [5] A. K. Saha, G. Biswas, and K. Muralidhar, Three-dimensional study of flow past a square cylinder at low Reynolds numbers, *Int. J. Heat Fluid Flow* **24**, 54 (2003).

- [6] A. Sohankar, C. Norberg, and L. Davidson, Low Reynolds number flow around a square cylinder at incidence: Study of blockage, onset of vortex shedding and outlet boundary condition, *Int. J. Numer. Methods Fluids* **26**, 39 (1998).
- [7] M. Ozgoren, Flow structure in the downstream of square and circular cylinders, *Flow Meas. Instrum.* **17**, 225 (2006).
- [8] S. Dutta, K. Muralidhar, and P. Panigrahi, Influence of the orientation of a square cylinder on the wake properties, *Exp. Fluids* **34**, 16 (2003).
- [9] S. Dutta, P. K. Panigrahi, and K. Muralidhar, Experimental investigation of flow past a square cylinder at an angle of incidence, *J. Eng. Mech.* **134**, 788 (2008).
- [10] B. W. van Oudheusden, F. Scarano, N. P. Van Hinsberg, and D. W. Watt, Phase-resolved characterization of vortex shedding in the near wake of a square-section cylinder at incidence, *Exp. Fluids* **39**, 86 (2005).
- [11] B. W. van Oudheusden, F. Scarano, N. P. Van Hinsberg, and E. W. M. Roosenboom, Quantitative visualization of the flow around a square-section cylinder at incidence, *J. Wind Eng. Ind. Aerodyn.* **96**, 913 (2008).
- [12] X. H. Tong, S. C. Luo, and B. C. Khoo, Transition phenomena in the wake of an inclined square cylinder, *J. Fluid. Struct.* **24**, 994 (2008).
- [13] R. F. Huang, B. H. Lin, and S. C. Yen, Time-averaged topological flow patterns and their influence on vortex shedding of a square cylinder in crossflow at incidence, *J. Fluid. Struct.* **26**, 406 (2010).
- [14] D.-H. Yoon, K.-S. Yang, and C.-B. Choi, Heat transfer enhancement in channel flow using an inclined square cylinder, *J. Heat Transfer* **131**, 074503 (2009).
- [15] M. A. Moussaoui, M. Jami, A. Mezrhab, and H. Naji, MRT-lattice Boltzmann simulation of forced convection in a plane channel with an inclined square cylinder, *Int. J. Therm. Sci.* **49**, 131 (2010).
- [16] I. P. Castro and A. G. Robins, The flow around a surface-mounted cube in uniform and turbulent streams, *J. Fluid Mech.* **79**, 307 (1977).
- [17] J. C. R. Hunt, C. J. Abell, J. A. Peterka, and H. Woo, Kinematical studies of the flows around free or surface-mounted obstacles; applying topology to flow visualization, *J. Fluid Mech.* **86**, 179 (1978).
- [18] R. P. Hosker, Flow and diffusion near obstacles, in *Atmospheric Science and Power Production*, edited by D. Randerson, U.S. Department of Energy Report No. DOE/TIC-27601, USDOE Technical Information Center, Oak Ridge, TN, 1984, Chap. 7, p. 241.
- [19] R. Raul, P. S. Bernard, and F. T. Buckley, An application of the vorticity-vector potential method to laminar cube flow, *Int. J. Numer. Methods Fluids* **10**, 875 (1990).
- [20] R. Raul and P. S. Bernard, A numerical investigation of the turbulent flow field generated by a stationary cube, *J. Fluid. Eng.* **113**, 216 (1991).
- [21] A. K. Saha, Three-dimensional numerical simulations of the transition of flow past a cube, *Phys. Fluids* **16**, 1630 (2004).
- [22] A. K. Saha, Three-dimensional numerical study of flow and heat transfer from a cube placed in a uniform flow, *Int. J. Heat Fluid Flow* **26**, 80 (2006).
- [23] L. Klotz, S. Goujon-Durand, J. Rokicki, and J. E. Wesfreid, Experimental investigation of flow behind a cube for moderate Reynolds numbers, *J. Fluid Mech.* **750**, 73 (2014).
- [24] M. H. Khan, A. Sharma, and A. Agrawal, Simulation of flow around a cube at moderate Reynolds numbers using the lattice Boltzmann method, *J. Fluid. Eng.* **142**, 011301 (2020).
- [25] M. H. Khan, H. H. Khan, A. Sharma, and A. Agrawal, Laminar vortex shedding in the wake of a cube, *J. Fluid. Eng.* **142**, 111301 (2020).
- [26] A. Richter and P. A. Nikrityuk, New correlations for heat and fluid flow past ellipsoidal and cubic particles at different angles of attack, *Powder Technol.* **249**, 463 (2013).
- [27] A. Hölzer and M. Sommerfeld, Lattice Boltzmann simulations to determine drag, lift and torque acting on non-spherical particles, *Comput. Fluids* **38**, 572 (2009).
- [28] S. Sengupta, M. H. Khan, V. K. Veluri, P. K. Vijayan, A. Agrawal, and S. Bhattacharya, PIV investigations on the turbulent mixing of two opposing flows inside a scaled chimney model of a research reactor, *Exp. Therm. Fluid Sci.* **63**, 115 (2015).
- [29] I. Ashraf, A. Agrawal, M. H. Khan, P. Sooraj, A. Srivastava, and A. Sharma, Thrust generation and wake structure for flow across a pitching airfoil at low Reynolds number, *Sadhana* **40**, 2367 (2015).

- [30] P. Sooraj, M. H. Khan, A. Sharma, and A. Agrawal, Wake analysis and regimes for flow around three side-by-side cylinders, *Exp. Therm. Fluid Sci.* **104**, 76 (2019).
- [31] W. Thielicke and E. J. Stamhuis, PIVlab—Time-resolved digital particle image velocimetry tool for MATLAB, version 1.32, 2014.
- [32] W. Thielicke and E. J. Stamhuis, PIVlab—Towards user-friendly, affordable and accurate digital particle image velocimetry in MATLAB, *J. Open Res. Softw.* **2**, e30 (2014).
- [33] E. Lazar, B. DeBlauw, N. Glumac, C. Dutton, and G. Elliott, A practical approach to PIV uncertainty analysis, in *Proceedings of the 27th AIAA Aerodynamic Measurement Technology and Ground Testing Conference, Chicago, 2010* (AIAA, Chicago, 2010), p. 4355.
- [34] P. Holmes, J. L. Lumley, and G. Berkooz, *Turbulence, Coherent Structures, Dynamical Systems and Symmetry* (Cambridge University Press, Cambridge, 1998).
- [35] L. Sirovich, Turbulence and the dynamics of coherent structures. I. Coherent structures, *Q. Appl. Math.* **45**, 561 (1987).
- [36] H. Chen, D. L. Reuss, D. L. S. Hung, and V. Sick, A practical guide for using proper orthogonal decomposition in engine research, *Int. J. Engine Res.* **14**, 307 (2013).
- [37] A. Chatterjee, An introduction to the proper orthogonal decomposition, *Curr. Sci.* **78**, 808 (2000).
- [38] D. F. G. Durao, M. V. Heitor, and J. C. F. Pereira, Measurements of turbulent and periodic flows around a square cross-section cylinder, *Exp. Fluids* **6**, 298 (1988).
- [39] A. E. Perry and M. S. Chong, A description of eddying motions and flow patterns using critical-point concepts, *Annu. Rev. Fluid Mech.* **19**, 125 (1987).
- [40] J. Zhou, R. J. Adrian, S. Balachandar, and T. M. Kendall, Mechanisms for generating coherent packets of hairpin vortices in channel flow, *J. Fluid Mech.* **387**, 353 (1999).
- [41] R. J. Adrian, K. T. Christensen, and Z.-C. Liu, Analysis and interpretation of instantaneous turbulent velocity fields, *Exp. Fluids* **29**, 275 (2000).
- [42] H. H. Khan, S. F. Anwer, N. Hasan, and S. Sanghi, The organized motion of characterized turbulent flow at low Reynolds number in a straight square duct, *SN Appl. Sci.* **2**, 763 (2020).
- [43] J. Yang, M. Liu, G. Wu, H. Gu, and M. Yao, On the unsteady wake dynamics behind a circular disk using fully 3D proper orthogonal decomposition, *Fluid Dyn. Res.* **49**, 015510 (2017).
- [44] B. Lu and M. B. Bragg, Experimental investigation of the wake-survey method for a bluff body with a highly turbulent wake, *Proceedings of the 20th AIAA Applied Aerodynamics Conference, St. Louis, 2002* (AIAA, St. Louis, Missouri, 2002), paper 2002-3060.
- [45] D. G. Bohl and M. M. Koochesfahani, MTV measurements of the vortical field in the wake of an airfoil oscillating at high reduced frequency, *J. Fluid Mech.* **620**, 63 (2009).
- [46] A. Hölzer and M. Sommerfeld, New simple correlation formula for the drag coefficient of non-spherical particles, *Powder Technol.* **184**, 361 (2008).
- [47] J. Almedeij, Drag coefficient of flow around a sphere: Matching asymptotically the wide trend, *Powder Technol.* **186**, 218 (2008).